AGU PUBLICATIONS

JGR

Journal of Geophysical Research: Oceans

RESEARCH ARTICLE

10.1002/2016JC012271

Key Points:
- Deep western boundary current in the subpolar North Atlantic
- Quasi-decadal variations of deep circulation
- Deep transports related to NAO forcing

Correspondence to:
R. Zantopp,
rzantopp@geomar.de

Citation:
Zantopp, R., J. Fischer, M. Visbeck, and J. Karstensen (2017), From interannual to decadal: 17 years of boundary current transports at the exit of the Labrador Sea, *J. Geophys. Res. Oceans*, *122*, doi:10.1002/2016JC012271.

Received 23 AUG 2016
Accepted 3 FEB 2017
Accepted article online 9 FEB 2017

© 2017. The Authors.
This is an open access article under the terms of the Creative Commons Attribution-NonCommercial-NoDerivs License, which permits use and distribution in any medium, provided the original work is properly cited, the use is non-commercial and no modifications or adaptations are made.

From interannual to decadal: 17 years of boundary current transports at the exit of the Labrador Sea

R. Zantopp[1], J. Fischer[1], M. Visbeck[1,2], and J. Karstensen[1]

[1]GEOMAR Helmholtz Centre for Ocean Research Kiel, Kiel, Germany, [2]Kiel University, Kiel, Germany

Abstract Over the past 17 years, the western boundary current system of the Labrador Sea has been closely observed by maintaining the 53°N observatory (moorings and shipboard station data) measuring the top-to-bottom flow field offshore from the Labrador shelf break. Volume transports for the North Atlantic Deep Water (NADW) components were calculated using different methods, including gap filling procedures for deployment periods with suboptimal instrument coverage. On average the Deep Western Boundary Current (DWBC) carries 30.2 ± 6.6 Sv of NADW southward, which are almost equally partitioned between Labrador Sea Water (LSW, 14.9 ± 3.9 Sv) and Lower North Atlantic Deep Water (LNADW, 15.3 ± 3.8 Sv). The transport variability ranges from days to decades, with the most prominent multiyear fluctuations at interannual to near decadal time scales (±5 Sv) in the LNADW overflow water mass. These long-term fluctuations appear to be in phase with the NAO-modulated wind fluctuations. The boundary current system off Labrador occurs as a conglomerate of nearly independent components, namely, the shallow Labrador Current, the weakly sheared LSW range, and the deep baroclinic, bottom-intensified current core of the LNADW, all of which are part of the cyclonic Labrador Sea circulation. This structure is relatively stable over time, and the 120 km wide boundary current is constrained seaward by a weak counterflow which reduces the deep water export by 10–15%.

1. Introduction

The Labrador Sea, located between Labrador and Greenland, is considered one of the prominent areas of open ocean convection and wintertime water mass transformation in the world's ocean [*Marshall and Schott*, 1999]. The general consensus in the scientific community regarding these two processes has been that enhanced convection (like in the early 1990s) would lead to larger than normal formation of Labrador Sea Water which in turn would be exported from the Labrador Sea through the Deep Western Boundary Current (DWBC). Just recently, and following a decade of rather weak convection, the Labrador Sea experienced two extreme winters during which convection once again reached depths of almost 2000 m [*Yashayaev and Loder*, 2009; *Kieke and Yashayaev*, 2015]. These occurrences coupled with the fact that a 17 year long time series of transports is now available at the exit of the Labrador Sea near 53°N, downstream of the convection area where the three components (Labrador Sea Water (LSW), North-East Atlantic Deep Water (NEADW), and Denmark Strait Overflow Water (DSOW) of the North Atlantic Deep Water (NADW)) merge into the DWBC, enable us to address a number of questions, such as the relationship between Labrador Sea convection and variability of boundary currents, or export, in different water mass layers. The deep western boundary current is the lower limb of the AMOC (Atlantic Meridional Overturning Circulation) [*Lozier et al.*, 2016] and as such is responsible for a significant part of the poleward ocean heat transport. In a gradually warming world, AMOC model simulations suggest a weakening of these transports by 30% [*IPCC*, 2013]. Sustained observations of the strength of the boundary currents are one way of directly verifying these predictions in the future.

During recent decades, the research into the AMOC (Figure 1) was focused on the variability of Labrador Sea Water formation [*Rhein et al.*, 2007; *Kieke et al.*, 2009], as this formation was intimately linked to the buoyancy forcing over the Labrador Sea. On the other hand, the even deeper part of the AMOC originating from north of the Greenland-Iceland-Scotland Ridge has received much less attention, presumably due to the fact that the overflow transports at the sill depth have been remarkably stable [*Jochumsen et al.*, 2015; *Hansen and Østerhus*, 2007]. No long-term trends or variations have been detected in the time series of those transports.

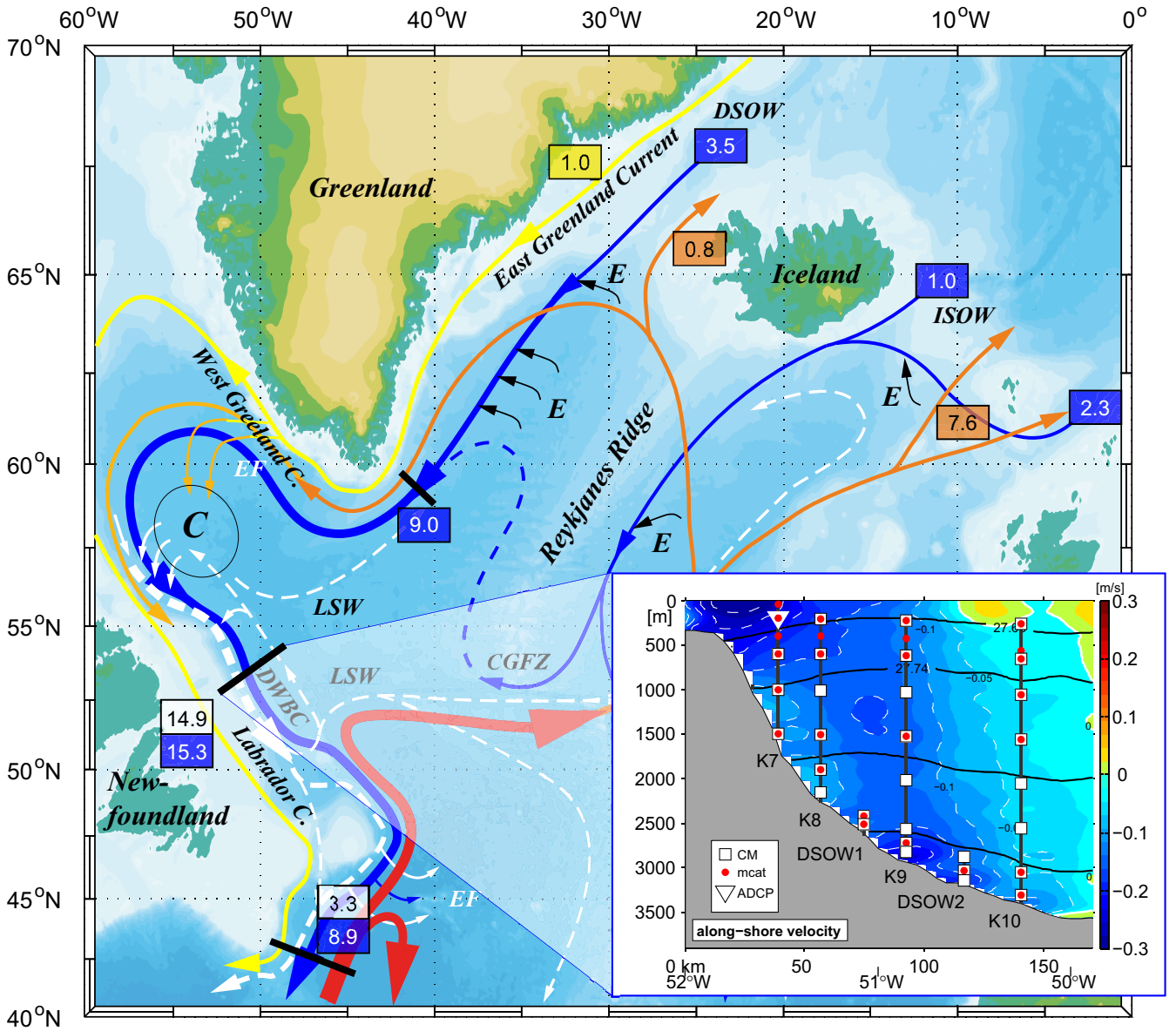

Figure 1. Overview map of the subpolar North Atlantic, with superimposed schematic paths of the Gulf Stream/North Atlantic Current (red) and components of the Deep Western Boundary Current (blue), plus transport estimates (in Sv) for the respective current components (colored boxes; LSW transports in white; LNADW transport in blue). The inset at the bottom right is the configuration of the moored array at 53°N for the 2012–2014 deployment, superimposed over the outflow and density fields obtained from shipboard LADCP and CTD stations for 1997–2014.

The two overflow water masses (NEADW, DSOW) merge in the Irminger Sea and the LNADW volume increases considerably through entrainment of ambient water. The DSOW reveals a relatively stable mean transport around 3.4 Sv [*Jochumsen et al.*, 2012] and a similar volume transport of 3.0 Sv is observed leaving the Nordic Seas east of Iceland [*Hansen et al.*, 2010]. These water masses contribute to the DWBC transport near Cape Farewell where *Bacon and Saunders* [2010] estimated 9 Sv of LNADW transport within the DWBC. This is considerably less than the estimate of 15 Sv in the Labrador Sea by *Fischer et al.* [2010] for the same density range; this apparent discrepancy will be discussed in section 4.1.

The 53°N observatory (see Figure 1, inset), measured at high temporal resolution, allows us to observe all of the deep water masses simultaneously through a top-to-bottom current meter array, which in turn permits the determination of transport time series, the characteristics of their inherent variability at different time scales, and their relationship with large scale atmospheric forcing and convection in the Labrador Sea.

Earlier publications with this data set focused on fractions of the time series in which full array coverage allowed the calculation of transports [*Fischer et al.*, 2004, 2010; *Dengler et al.*, 2006]. Subsequent investigations concentrated on intraseasonal time scales in comparison with data from other mooring efforts along the western boundary of the subpolar North Atlantic [*Fischer et al.*, 2015] and in comparison with high-resolution model data [*Böning et al.*, 2006; *Xu et al.*, 2013].

In this paper we focus on transport calculations and discuss several aspects related to data processing, comparisons and uncertainty estimates of the shipboard and moored measurements, and the use of statistical methods to overcome sparse data coverage. Final products are the time mean and fluctuating transports in different water mass regimes and their relationship to the North Atlantic Oscillation (NAO), convection, and wind forcing. The result of this work is a unique set of top-to-bottom boundary current transport time series in a key area of the subpolar Meridional Overturning Circulation (MOC), and we invite the scientific community to use these results for further analysis, model evaluations, and comparison to other observational evidence of deep subpolar circulation variability. Section 2 describes the data and data processing used, and sections 3 and 4 present the results of this study regarding the mean and time varying transports and their connection to other regional signals. An outlook and linkage of this effort to ongoing observational programs will also be provided in section 5.

2. Data and Data Processing

2.1. The 53°N Moored Observatory

For more than a decade and a half, from 1997 to 2014, and currently ongoing, the moored array at 53°N was deployed over varying time intervals and spatial configurations. In addition to the mooring work, there were 13 full surveys of hydrography and currents at the boundary. These were obtained by shipboard stations with CTD/LADCP measurements during the mooring service cruises (typically every other year, see Table A1 in Appendix).

The chronological evolution of the entire 53°N array versus water depth (left-hand scale) and distance (right-hand scale) is shown in Figure 2, where mooring distances are calculated NE of 52°W which coincides with the longitude of the 300 m isobath (see Figure 1, inset). The historical background is as follows: Starting in 1997, an array of five moorings with a total of 25–30 instruments was deployed at about 53°N to measure the top-to-bottom structure of the outflow from the Labrador Sea. The moorings were originally identified as K7, K8, etc. as part of a larger moored measurement program in the subpolar North Atlantic. Instruments were strategically placed in the water column to adequately sample the main water masses

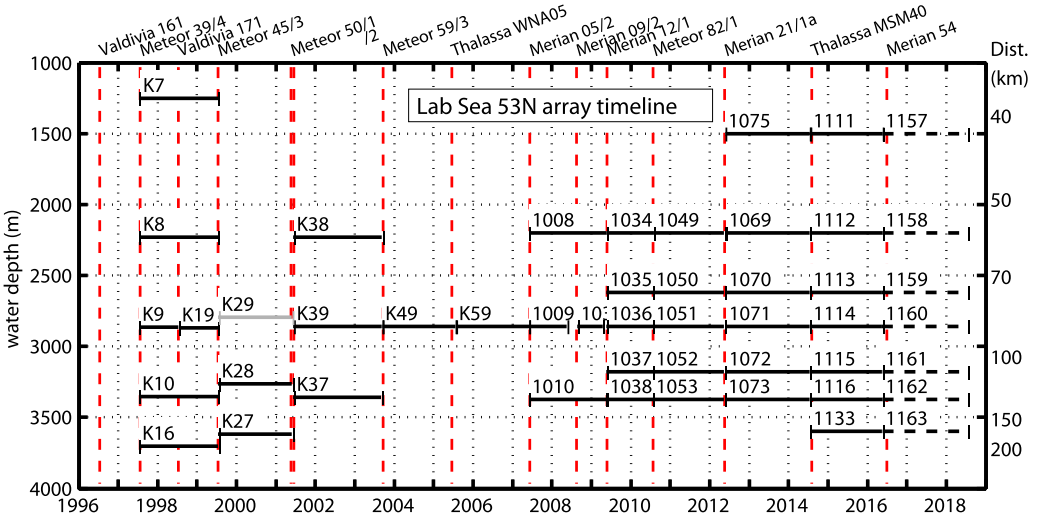

Figure 2. Timeline for the moored array at 53°N, oriented in a general direction toward 025° true. Dashed lines are moorings currently in water and scheduled for recovery in summer 2018. This analysis includes only data up to mid-2014. The gray-shaded mooring K29 (in 1999–2001) yielded only ADCP data above 300 m. Vertical red dashed lines represent mooring service cruises with name of the research vessel and cruise identifier at the top. Labels above the deployment period identify the respective mooring in the "Kiel" inventory.

(see section 2.3 and Figure 4), with additional emphasis on the bottom-intensified outflow of the Denmark Strait Overflow Water (DSOW). Subsequent deployment periods suffered some instrument losses and funding constraints, leading to significant gaps in data coverage (see period 2000–2007 in Figure 2). The array was again expanded in 2007, and in 2009 supplemented by additional near-bottom moorings to cover the deep core of the DSOW (moorings at distances of 79 and 117 km, water depths of 2620 and 3180 m, respectively). The central mooring, generally labeled K9, located at 92 km and a water depth of 2860 m, has the longest and most consistent data coverage and will be used as a baseline to estimate array-based transports for the more sparsely instrumented time period 2003–2007 (section 3.2.3). The labels in Figure 2 identify the respective moorings by their "Kiel" inventory numbers.

Looking ahead, the most recent configuration in 2014–2016 (recovered but not yet included in this analysis) features a supplement of additional deep measurements offshore of K10 in order to improve the monitoring of the strength of the offshore recirculation (mooring 1133 in Figure 2), i.e., the array constitutes an essential contribution to international collaboration efforts: an extension toward the continental shelf through the Canadian VITALS project (Ventilation, Interactions and Transports Across the Labrador Sea, http://knossos.eas.ualberta.ca/vitals/), as well as instrumentation for OSNAP (Overturning in the Subpolar North Atlantic Program) [*Lozier et al*., 2016] and trans-basin transport budgets.

2.2. Instrument Data Processing

As the basic processing of the current meter data has not changed since earlier publications, we refer to *Fischer et al*. [2004] and include only a brief description herein. The data are from different types of instruments, i.e., rotor current meters by Aanderaa (RCM-8), acoustic Doppler current meters by Sontek (Argonaut), and occasionally 75 kHz acoustic Doppler profilers by Teledyne/RDI. Raw current data were detided by applying a 40 h lowpass filter, and then subsampled to 12 hourly resolution. The 12 h data are rotated by 25° counterclockwise such that the main current component (averaged over the whole array) is along the isobaths (positive toward 335° true, negative toward 155° true, coinciding with the mean direction of the deep flow) and also the direction of the principle variance axis. The along-isobath component is then used for the subsequent transport calculations.

As a typical example of the velocity structure in the center of the boundary current (Mooring K9), we show a "stick plot," i.e., velocity vectors, detided and subsampled to 12 h resolution (Figure 3). The current meter depths typically range from 200 m down to 50 m above bottom. While the upper half of the water column is populated by strong eddy motion superimposed on a weaker mean outflow (out of the Labrador Sea in southeastward direction), the deeper part of the water column is much steadier with a strong, bottom-intensified outflow. This change in general flow characteristics occurs near the upper limit of the Lower North Atlantic Deep Water (LNADW), in this case between 1500 and 2000 m.

For a look at the longer time scales we present in Figure 3b the along-topography current from the deepest record (50 m above bottom near 2800 m) at the central mooring K9 (Figure 1, inset). This record shows very stable velocities around 26 cm/s in southeastward direction; i.e., outflow from the Labrador Sea. The flow is on average 2–5 cm/s stronger than the flow higher up near 2400 m, and the two records are correlated at $R = 0.96$. This illustrates that the vertical scales of the deep flow are resolved at the K9 location. It further shows that there is variability on interannual to decadal time scales, with two time periods (1999 and 2008/2009) that appear low relative to the long-term evolution of the time series.

In general the time series of the near-bottom currents exhibits two modes of variability: high-frequency motion which accounts for an rms difference of 5.5 cm relative to the red curve in Figure 3b which is due to the eddy like motion visible throughout the water column in Figure 3a. Besides the high-frequency variations, the red curve shows increased variability at periods on interannual and quasi-decadal time scales, together accounting for a standard deviation of 2.4 cm/s from the original time series.

2.3. Definition of Water Mass Boundaries and Their Variation

The central aim of this study is to calculate transports for deep water masses through integrating the flow field in density, temperature, and depth classes which is fairly straightforward if the entire array of instruments is available. Altogether, 13 CTD sections with some 150 profiles were obtained along the 53°N section between 1996 and 2014. We had to use these CTD station data as the hydrographic background because none of the deployments had moored temperature and salinity instrumentation adequate enough to determine water mass bounds. For obvious reasons, mooring work in the harsh Labrador Sea takes place during

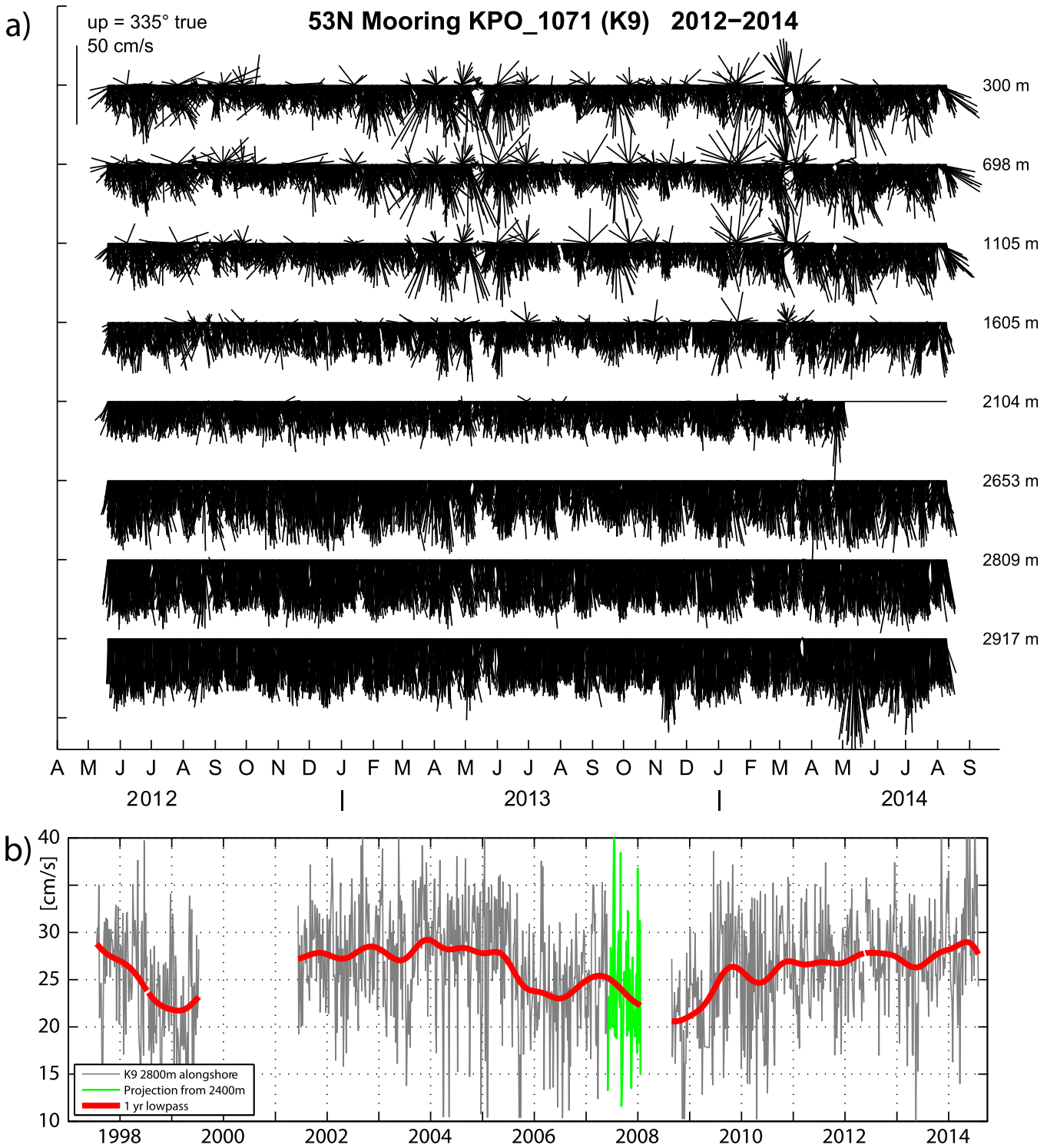

Figure 3. (a) Recent (2012–2014) current meter records in the center of the DWBC from mooring position K9. In this figure the currents are detided, subsampled and rotated by −25° to 335° true. (b) Long-term (1997–2014) alongshore component near 2800 m at station K9; gray for original data; green is extrapolated from the 2400 m record when the near-bottom instrument was lost, thick red is for the 1 year low-passed time series.

the summer months only, i.e., all cruises fall into the time window mid-May to late-September. Obvious concerns about the seasonality of the hydrographic surveys have been addressed by *Kopte* [2013] who found little to negligible seasonal signal in the deep layers of the Labrador Sea.

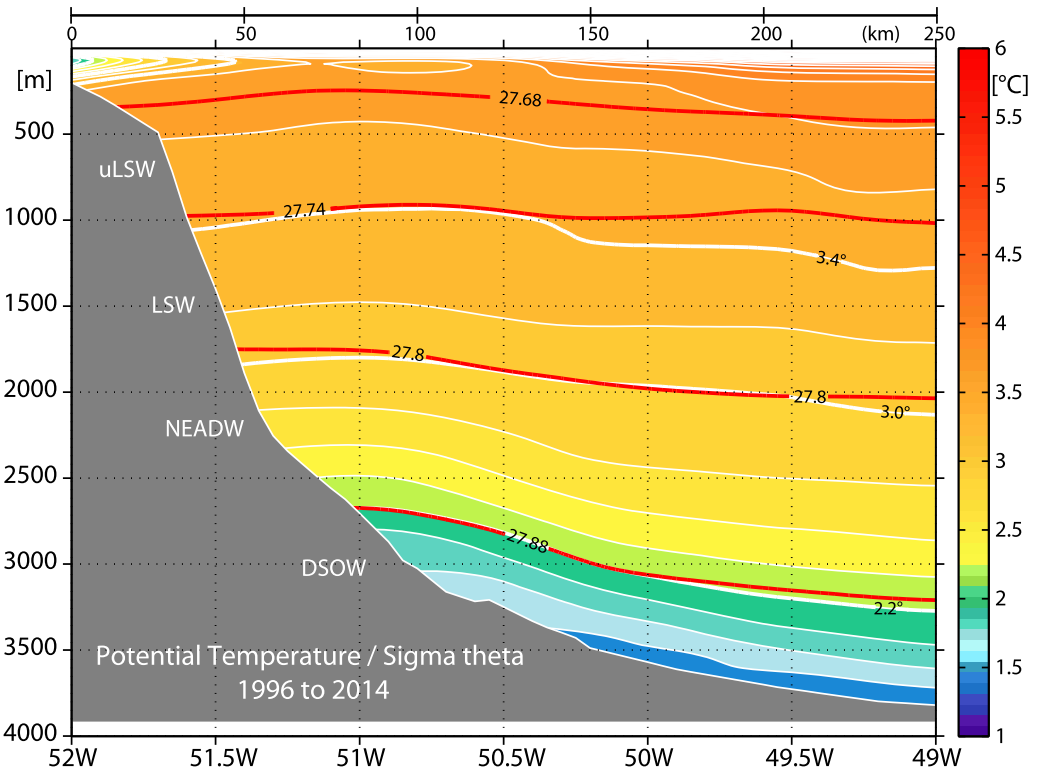

Figure 4. Averaged and gridded potential temperature distribution determined from CTD section data along the 53°N array. Water mass boundaries (as shown to the left of the boundary) are marked by isopycnals (potential density, heavy red lines) and the corresponding isotherms (potential temperature, heavy white lines).

Each of these sections was interpolated onto a grid with 10 m vertical resolution and 0.1° horizontal resolution in the range 52°W–49°W, using a Gaussian weighting with a half width of 30 m and cutoff radius of 150 m for the vertical interpolation, and 0.2° and 0.4° in longitude, respectively. A common topography, obtained during the "Merian" cruise 21/1a in 2012, was applied to all sections. The mean potential temperature distribution along 53°N is shown in Figure 4, with potential density superimposed which present one possible definition of the relevant water masses: $\sigma_\theta > 27.88$ kg m^{-3} for Denmark Strait Overflow Water (DSOW), above it the Northeast Atlantic Deep Water (NEADW) at $\sigma_\theta = 27.88$ kg m^{-3} to $\sigma_\theta = 27.80$ kg m^{-3}, followed by the Labrador Sea Water (LSW), $\sigma_\theta = 27.80$ kg m^{-3} to $\sigma_\theta > 27.74$ kg m^{-3} for the so-called classic LSW (cLSW), and finally the upper LSW (uLSW) in the range $\sigma_\theta = 27.74$–27.68 kg m^{-3} (Figure 4). The latter is subject to winter-time mixing and rather strong seasonality not represented in the summer sections.

For a second set of water mass definition, we observe that the deep boundaries can be described equally well by potential temperature (θ), a parameter that—compared to salinity/density—could be more reliably compared to measurements within the moored array. In comparison the density surface $\sigma_\theta = 27.88$ kg m^{-3} corresponds to $\theta = 2.2$°C, while $\sigma_\theta = 27.80$ kg m^{-3} corresponds to $\theta = 3.0$°C.

A third option to determine the transports uses depth layers which is important for several reasons: First, this definition allows us to evaluate the transport variations solely due to variations in velocity, separate from any layer thickness modulation that might have occurred over time. Second, while the current meter records allow a separation of high-frequency noise (generated for example through Topographic Rossby Waves (TRWs)) [*Fischer et al*., 2015] and the sought-after long-term variations, the hydrographic data are subject to contaminations by these processes. Thus, the layer thicknesses are subject to not only property changes, but also to dynamically induced thickness variations (mainly those of the intraseasonal variations that appear as quasi-synoptic snapshots in any of the hydrographic sections).

The most important boundary in this context is the one that separates the LSW from the LNADW, and we will look at this in more detail (Figure 5). From the distance of individual estimates relative to the mean location of the bounding isopycnal we estimate an overall rms deviation of 162 m for the depth of

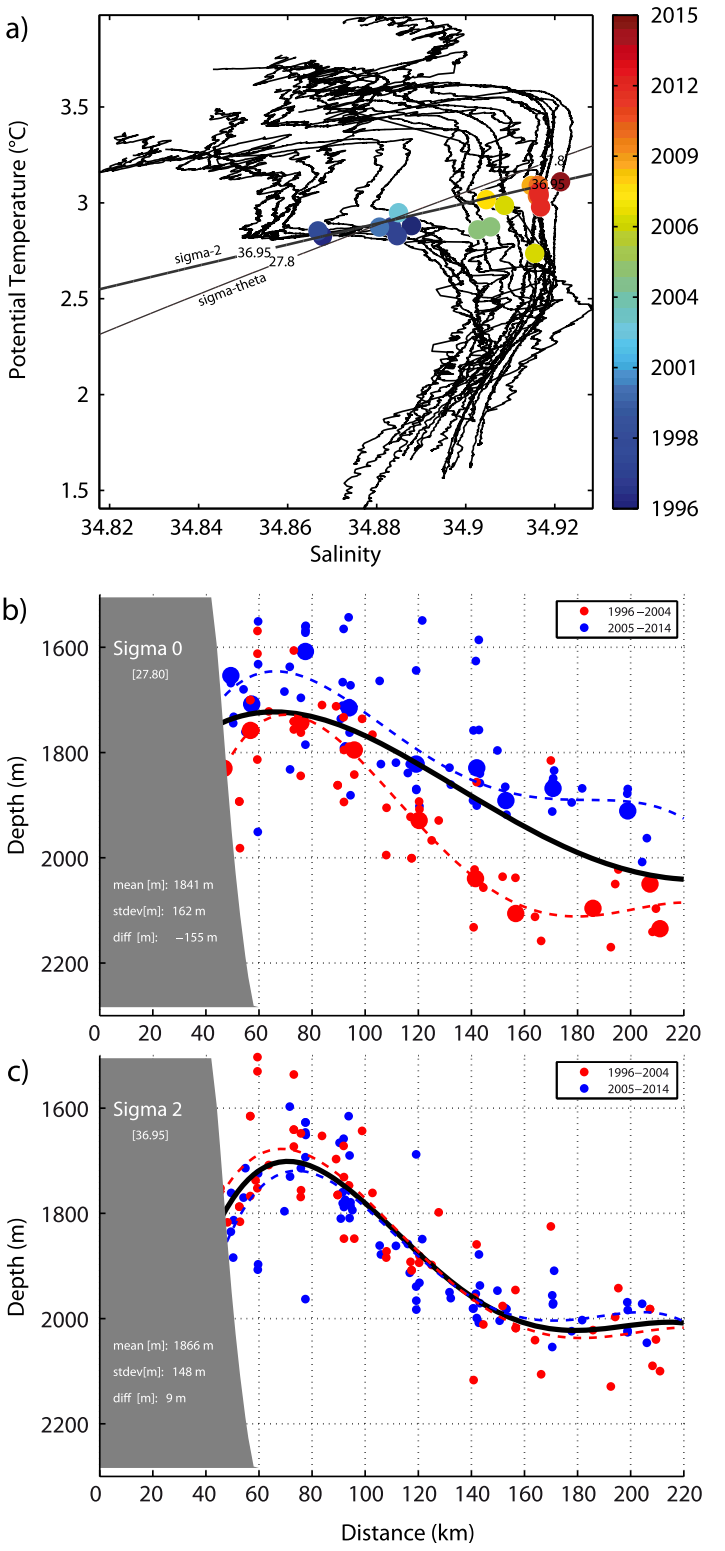

Figure 5. (a) T/S diagram at mooring location K9 (DWBC center) from 13 ship cruises from 1996 to 2014. Colored dots mark the 1850 m depth in T/S space. Also included are densities $\sigma_\theta = 27.80$ kg m^{-3} and $\sigma_2 = 36.95$ kg m^{-3} (referenced to 2000 m depth). Location of the isopycnal boundary between LNADW and LSW for all stations along the boundary current array for (b) $\sigma_\theta = 27.80$ kg m^{-3} and for (c) $\sigma_2 = 36.95$ kg m^{-3}. Different colors are for different time periods (see legend in the graph).

$\sigma_\theta = 27.80$ kg m^{-3}, and this scatter has basically two sources: There is a long-term signal visible by comparison of the red versus the blue stations in a way such that the LNADW expands upward by almost 170 m from the first to the second half of the observational period, while the cLSW shrinks during the same time period. The second contribution is most probably through TRWs which are in geostrophic balance and therefore impact the density structure; individual sections are random, quasi-synoptic snapshots of the TRWs. It thus becomes clear that an accurate temporal evolution of the density field cannot be estimated from just a few summer station data. However, when using a more local reference for the isopycnic boundary, namely $\sigma_2 = 36.95$ kg m^{-3} (Figure 5c; referenced to 2000 m) the temporal depth variation is absent while the TRW scatter is about the same. This rather surprising effect comes from the large change of the TS evolution during the previous decades. This behavior has the advantage that we are able to use the mean location of the well-defined $\sigma_2 = 36.95$ kg m^{-3}, and all transport variations (longer than say 90 days) can be determined from velocity variations alone.

3. Determination of DWBC Transports From Moored and Station Data

The main objective of this paper is to determine the export of NADW and its constituents from the Labrador

Sea by the DWBC. Ideally, one would use external information of the velocity covariance matrix to interpolate the moored records to a regular grid by some sort of objective mapping procedure. However, as such information is not available we decided to use a less complex procedure to map the mooring data by two-dimensional Gaussian interpolation (see section 3.2.1). LADCP data, as described below, are used to supplement the velocity field at the Labrador shelf break and the offshore location near 200 km.

3.1. LADCP-Gridded Velocity Field and Accuracy Considerations

On each of the 13 mooring service cruises between the summers of 1996 and 2014 we continuously operated a vessel-mounted ADCP and combined its data with on-station full ocean depth velocities from CTD/LADCP casts. This allows us to address three issues:

1. The spatial resolution of the LADCP data set is significantly higher than that of the moored array (typically 12–15 stations across the array compared to 3–5 moorings). The LADCP data thereby provide an estimate of the vertical and horizontal scales which are needed for interpolation of the moored data onto a regular grid and subsequent transport integration.
2. The LADCP station data typically exceed the moored array seaward into the deep basin and thus offer a first estimate of the magnitude of the recirculation cells adjacent to the DWBC [*Lavender et al.*, 2000; *Fischer and Schott*, 2002].
3. We use the termination of the DWBC in the LADCP data as the onshore/offshore boundary condition of the moored fields.

The interpolated and gridded mean velocity section from the combined shipboard data for the entire period (1996–2014) is shown in Figure 6. Near the surface, the flow at the edge of the Labrador shelf break exhibits the Labrador Current (LC) extending down to about 500 m. Below, and hugging the topography, is a clear velocity minimum that extends from about 2000 m up to the surface offshore of the LC, thereby separating the LC from the DWBC. Seaward, the flow structure is more barotropic, with low shears in the LSW

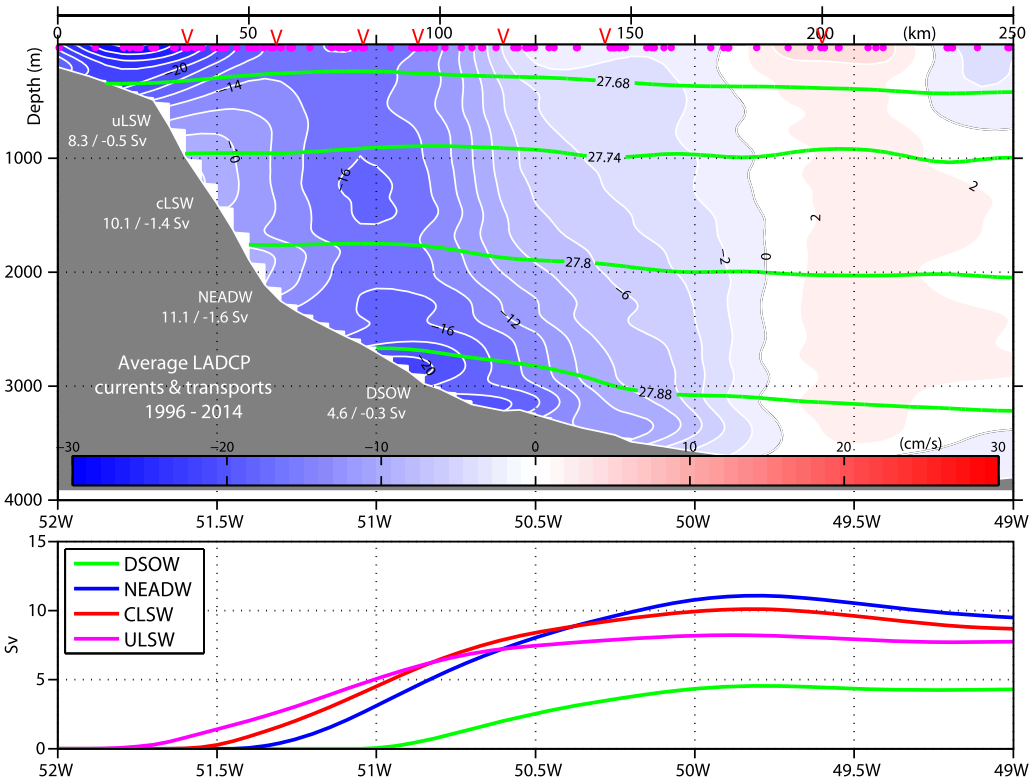

Figure 6. Boundary current section at 53°N derived from 150 LADCP stations in 1996–2014. Blue color is for outflow from the Labrador Sea along the topography (units in cm s^{-1}). Isopycnic levels (green) were used to distinguish the deep water masses and to calculate transports. DWBC transports are calculated from the topography out to the current reversal, and recirculation transport from zero crossing out to 49°W. The zero isotach is highlighted in grey. Lower graph shows cumulative transports for each of the deep water layers. Mooring positions are marked by red symbols (V) at the top.

range, and this part of the DWBC is terminated by the current reversal (directed into the Labrador Sea) offshore of 50°W. Underneath the LSW, and associated with the overflow contributions to the DWBC, we see a bottom intensification of the flow (see also the stick plots in Figure 3a). This pronounced current plume is characterized by very stable velocities, with maximum speeds sometimes reaching 40 cm/s, and annual averages of typically 25 cm/s (Figure 3b). The configuration of the deep current plume follows the slope of the shelf and is thus displaced offshore, resulting in a slanted structure of the DWBC. The spatial scales deduced from the LADCP flow fields verify that the moored array is capable of resolving the major features of this flow field, with typical horizontal scales of 50–100 km, and vertical scales of several hundred meters to more than 1000 m in the LSW range. Thus, the scales of the flow field are adequately resolved by the moored array if the full set of moored stations is in place. However, limitations occur right at the edges of the boundary current, and composite (mean) LADCP data are used to supplement the mooring data by introducing a virtual "zero-crossing" mooring in the recirculation regime (at 200 km).

The gridded flow fields allow easy integration and determination of transports. Multiplying the grid dimensions with the interpolated current yields transport per grid cell, and subsequent integration then allows the determination of transports within the water mass boundaries, as well as cumulative transports from the topography into the basin (Figure 6). We define the DWBC transport as the maximum transport out of the Labrador Sea (generally from the topography out to the zero isotach).

While the DWBC transport is best estimated by the mooring data supplemented by LADCP information, the offshore recirculation [see *Lavender et al*., 2000] is solely determined from the station data. The recirculation transport is defined in a range from the DWBC edge out to 49°W, about 80 km wide. Recirculation speeds are generally low, just a few cm/s, equally supported by individual float trajectories [*Fischer and Schott*, 2002], and although the width of the recirculation regime is comparable to the DWBC, its transport is generally much weaker, about 2 Sv each for the layers above and below the boundary between LSW and LNADW, which is on the order of 10–20% of the total DWBC transport (for transport numbers see Figure 6)

An interesting question is how accurate and robust the LADCP-based DWBC transports are based on the limited number of sections and the large scatter due to TRW variability. An error estimate based on a Monte Carlo test with data subsets shows robust transport numbers on the basis of at least 65% of the data. Then the uncertainties (2 times the standard deviation, 95% significance) are of the order of 2.8–3.0 Sv for each of the layers (LSW and LNADW). For details of the error estimates see section A3.1.

3.2. Transport Calculations From Moored Records

The calculation of transport time series has to follow different routes depending on the station and instrument coverage by the array that is illustrated in Figure 7. In the early stage of the investigation we had a full boundary current array with stations throughout the horizontal extent of the boundary current and instruments from near surface to the bottom. This coverage has been used throughout the later decade of the array from 2007 to present (periods highlighted in red in Figure 7). In these periods the instrument density was sufficient for interpolating the velocity records to a regular grid and integrating the gridded field to obtain transports in water mass classes.

However, from mid-2003 to mid-2007, only the central mooring K9 was in place. In order to obtain layer transports during this period (green in Figure 7), we estimated the relation between layer transports and K9 velocity records during periods with full array coverage (red in Figure 7). Thus, we obtain a set of transfer coefficients to project the equivalent records during the "green" period to layer transports (section 3.2.3).

Then there were periods where the central mooring was not in place. These periods were of different lengths: a gap of 2 years occurred when moorings broke loose in mid-1999, and shorter gaps during mooring turnaround. For these periods we tested several procedures to fill the gaps, and we finally decided to use an iterative EOF technique called Singular Spectrum Analysis (SSA-gap filling, see section 4.3).

3.2.1. Mapping the Current Field by Gaussian Interpolation

As a first step to integrate the current field, we interpolated the along-isobath currents to an equidistant grid with cell sizes of 2 km horizontally and 20 m vertically. The interpolation onto these grid points uses Gaussian weighting, with different horizontal and vertical scales: half-width (25 km) and maximum influence (80 km) radii were chosen on the basis of the LADCP analysis; similarly we used vertical scales of 500 m and 1200 m, respectively. These scales were slightly increased to (40, 120 km) and (600, 1500 m), respectively,

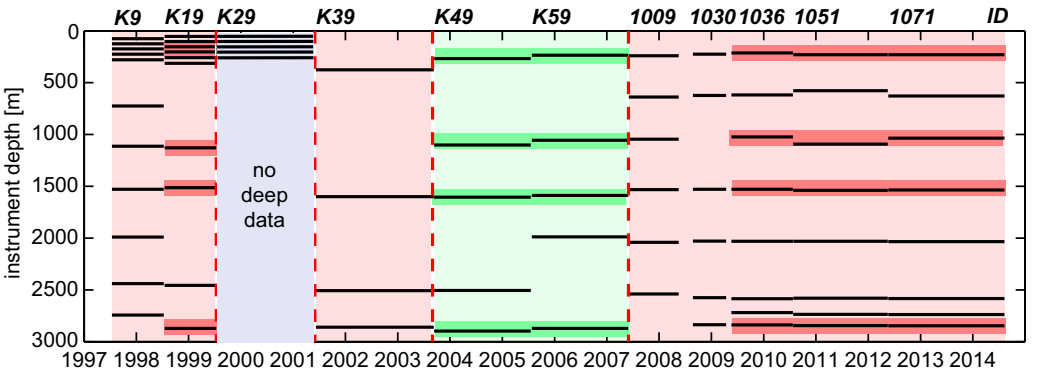

Figure 7. Selection of current meter levels from full-coverage array (red) for transports regressed from single mooring coverage (green). Mooring IDs for the central mooring K9 (see also timeline in Figure 2) are listed at the top. The gray-shaded mooring K29 (1999–2001) yielded only ADCP data above 300 m.

for those time periods with sparse instrumentation (2001–2003, 2007–2009). This then allows later evaluation of mapping scales to the uncertainty of the gridded velocity pattern (see Appendix with error analysis).

The first attempt to map the velocity field was performed with the long-term mean flow from both the moored array, and the LADCP flow field (Figure 8). Both fields have their inherent advantages, namely, the strong reduction of intraseasonal noise through long-term averaging in the mooring data, and the better horizontal coverage by the station data especially at the edges (inshore and offshore) of the array. Thus, we decided to combine the two fields in these areas, by terminating the gridded flow field by a mean, but rather weak flow from the LADCP pattern.

In analogy, this procedure was applied to annual mean flow fields and is shown under the results section in Figure 9.

3.2.2. Integration of the Gridded Flow Field to Obtain Transports

From the gridded fields it is straightforward to determine volume transports for various layers. First of all, the velocities in each grid cell were multiplied by the size of the cell, giving a transport per grid cell in m^3 s^{-1}. The integration (summing up) is then performed in depth layers, in isopycnic layers (both σ_θ and σ_2, see above), and thermal bounds or limited by the seafloor. Here the uncertainties in transport calculations introduced by bottom triangles are higher for the DSOW than in the layers above.

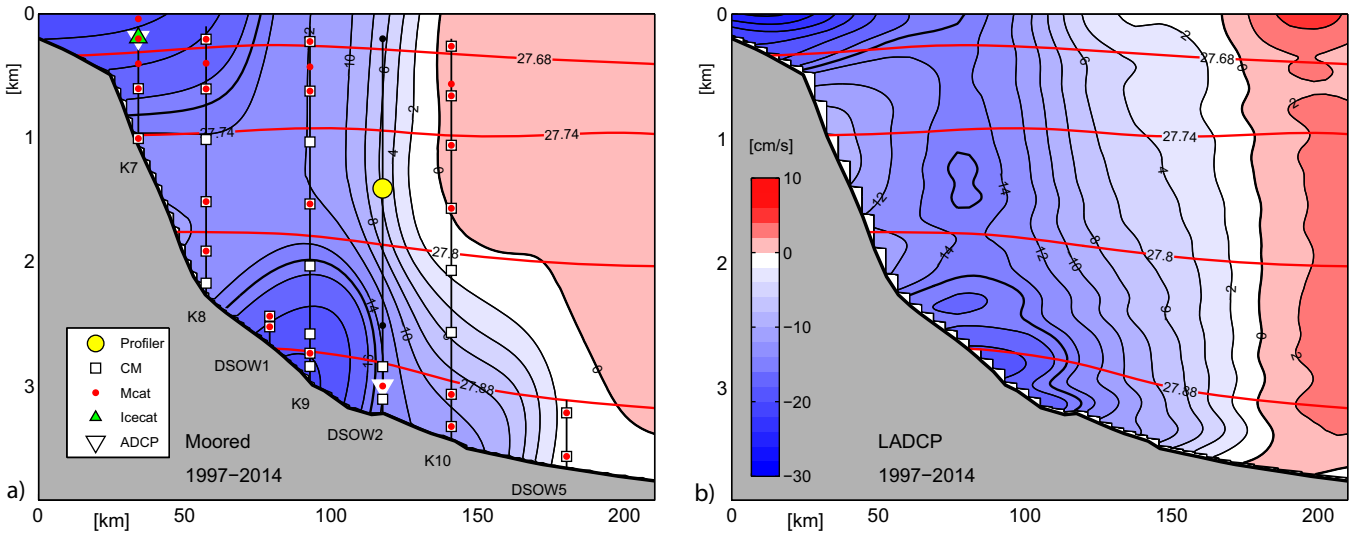

Figure 8. Long-term mean of outflow velocity at 53°N from moored (left) and shipboard (right) observations. The lines in Fig. 8a indicate the mooring locations with the recent (2014) instrumentation; the red lines are the isopycnals separating the water masses.

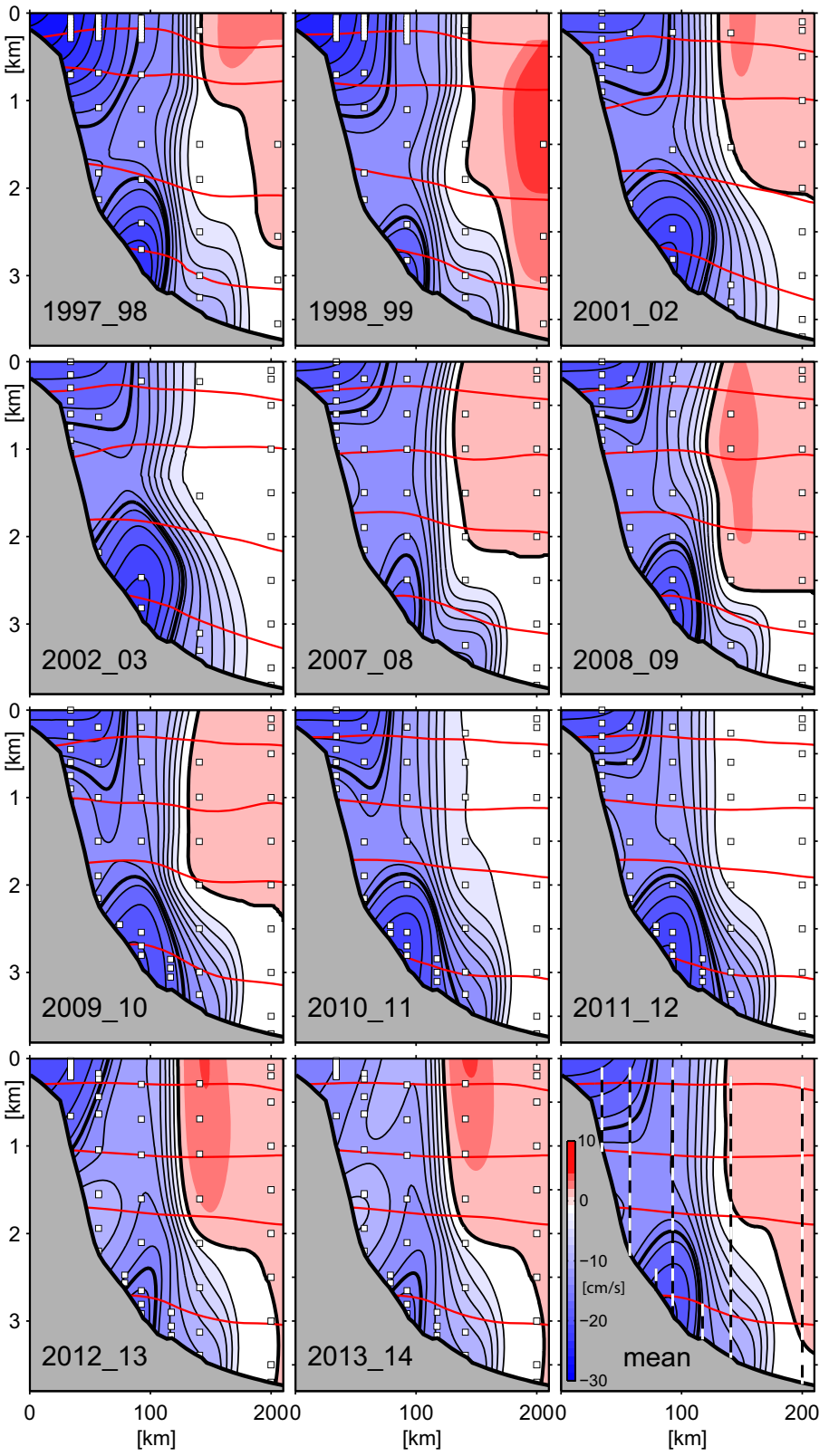

Figure 9. Annual mean sections of Labrador Sea outflow from moored observations at 53°N. Each section is a 1 year mean (midsummer to midsummer, as indicated). Instrument locations are indicated by small squares; seaward (at 200 km) and shoreward dots are from average LADCP records except for the periods 1997–1999 and 2012–2014 when moored records were available. Superimposed are the isopycnals (σ_θ) from the mean hydrography separating the different water masses.

3.2.3. Regression Method for Sparse Data Coverage

There are two deployment periods (2003–2005, 2005–2007) where only the central mooring (K9) yielded useful records. The challenge of recovering meaningful transport estimates from this limited coverage is addressed in Figure 7: The time periods highlighted in red had sufficient current meter coverage to obtain direct transport estimates—typically a full array has 20–25 current meters distributed to cover the main features of the deep boundary current of which 5–8 current meters are located in the central mooring. However there were periods (highlighted in green) during which there was only the central mooring in place. We calculated multiple linear regressions between the four continuous current meter locations at 200, 1100, 1500, and 2800 m and the respective transports for the time periods marked in darker red and used those multiple regression coefficients to transfer the respective velocity records marked in darker green into transports (Table A3). The resulting correlation coefficients are high (0.52 and 0.66) and significant at the 90% confidence level for LSW and NEADW. However, the rms difference between original and reconstructed transport time series for the period with full coverage is rather large (5 Sv) for LSW but relatively small for the NEADW layer (1.7 Sv).

The gain factors for different instrument levels, rms differences, and resulting correlation coefficients are shown in Table A4 in Appendix.

3.2.4. Gap Filling and Modal Decomposition

As most of the time series used herein have gaps of arbitrary occurrence and length, we fill these gaps prior to further analysis. The longest gaps of almost 2 year duration arose from a total loss of the central mooring K9; at two other instances we had moorings breaking loose a few months before their scheduled replacement, and the third kind of gap is short (less than 10 days) during the mooring exchange every other year. The gap filling aims for continuous and equidistant time series (5 day resolution) in which the statistics should not be altered significantly by the procedure. This was achieved through singular spectral analysis [*Ghil et al*., 2002; *Kondrashov and Ghil*, 2006].

The idea of SSA is to decompose a time series (here currents or volume transports) into oscillatory components and noise, even when the length of the time series must be considered short with respect to the time scales of interest (interannual to decadal). We will use this method to both fill the gaps of the respective time series and to determine the leading modes of variability in a noisy background field.

The method relies on basic linear algebra such as eigenvalue and eigenvector determination for a single univariate case represented by an individual time series of either current or transport. This method is summarized in the review paper by *Ghil et al*. [2002]. We herein use the SSA-MTM Toolkit, a free software package, specifically designed for performing SSA and other spectral analysis methods [*Vautard et al*., 1992]. The procedure involves the derivation of temporal EOFs and the use of singular value decomposition (SVD) which can only be applied to continuous records. Thus, an iterative procedure has been used in which the gaps are replaced by a first very crude estimate of the missing data in the gaps. EOFs are then calculated and a selected number of modes is used to reconstruct the time series as a secondary estimate—which is used to replace the original gaps. This step is then repeated for refinement, resulting in a gap-free time series in which the statistical parameters of the original time series have not been altered significantly (see Table A5 in Appendix). The gap filling uses a large number of modes (usually 20) in order to reproduce a realistic level of variability, whereas the analysis of the long time scales we are interested in uses only a few modes. Only a few low-order modes contain most of the variance (see section 4.3).

4. Mean and Variable Transports

4.1. Total and Annual Mean Transports

The main result of the herein described processing are annual mean estimates of the DWBC at the exit of the Labrador Sea, DWBC transports as total 17-year means and as annual averages in water mass classes, and complete transport time series at full 5 day resolution in all NADW ranges of the DWBC; this high temporal resolution allows the analysis of a wide frequency range, although the focus herein is on interannual to decadal time scales

In analogy to the procedure applied to the record length mean flow field we determined annual means of the DWBC flow (Figure 9). Sufficient coverage across the array to derive sections (and thus transports) is present for 11 different year-long periods, approximately from midsummer to midsummer of the following

year (see Figure 2). Only during the first 2 years, 1997–1999, the two most inshore and offshore moorings (K7, K16) were available to measure the flow. For the subsequent years, the long-term mean of the LADCP-derived section was used at these two locations to delimit the flow field. The basic structure of the Deep Labrador Current has several distinct features, namely a shallow Labrador Current (LC) at the shelf edge, and a current minimum right at the topography and underneath the LC. Then, further offshore the current structure is vertically unsheared (barotropic) throughout the LSW range, at time referred to in the literature as the Deep Labrador Current [e.g., *Lazier and Wright*, 1993]; and finally there is a bottom intensified current core covering both, the DSOW and the NEADW range. The DWBC is then terminated by a weak current reversal approximately 150 km off the shelf edge. In 3 of the 11 sections the offshore return flow is almost absent, i.e., the position of the zero isotach, and thus the width of the DWBC is not well defined, and it is only by adding information from the mean field that the DWBC edge is defined.

According to the analysis of the water mass definitions (section 2.3 and Figures 4 and 5), we decided to present annual mean transports in depth, density, and potential temperature definitions of the water mass bounds (Table 1); this would allow a direct comparison with other estimates in the subpolar North Atlantic. Corresponding to years for which we were able to produce the annual mean DWBC maps we were able to directly determine the annual mean transports in any of the layer definitions. Typically, the total NADW transport between 400 m depth and the bottom is of the order of 30 Sv with a total range of 24 Sv (2013/2014) to 36 Sv (1997/1998).

Table 1 also includes years when only the central mooring K9 was available—these years are highlighted in green and their transport uncertainty is 1.5 times larger than for years with full instrument coverage. For

Table 1. Annual Means of Volume Transports in Depth, Density, and Temperature Classes[a]

		Depth (m)					Density (kg m^{-3})				Temperature (°C)		
		>400	LSW	NEADW	DSOW	LNADW	LSW	NEADW	DSOW	LNADW	NEADW	DSOW	LNADW
		400–Bottom	400–1850	1850–2800	2800–Bottom	1850–Bottom	400–$\sigma_2 = 36.95$	$\sigma_\theta = 27.80$–27.88	$\sigma_\theta = 27.88$–Bottom	$\sigma_2 = 36.95$–Bottom	3.0–2.2	2.2–Bottom	3.0–Bottom
1997–1998	Mean	36.1	20.0	11.2	4.9	16.0	19.5	12.0	4.6	16.6	11.3	4.6	15.9
	SD	5.4	3.3	1.8	1.5	3.2	3.2	2.0	1.2	3.1	2.0	1.2	3.1
1998–1999	Mean	31.3	18.4	8.5	4.4	12.7	17.9	9.3	4.2	13.4	8.7	4.2	12.8
	SD	5.4	4.0	1.6	1.8	3.2	3.9	1.9	1.4	3.1	1.8	1.4	3.1
2001–2002	Mean	34.2	15.5	13.4	5.4	18.6	15.0	14.3	4.9	19.2	13.7	5.0	18.6
	SD	6.3	3.1	2.2	2.2	4.0	3.1	2.5	1.8	3.9	2.4	1.8	3.9
2002–2003	Mean	34.7	15.5	13.9	5.3	19.1	15.0	14.9	4.9	19.7	14.2	4.9	19.0
	SD	5.9	2.7	2.3	1.9	3.7	2.7	2.5	1.5	3.7	2.4	1.6	3.6
2003–2004	Mean	30.1	14.5	10.5	5.1	15.6	14.2	11.2	4.8	16.0	10.8	4.8	15.6
	SD	4.6	2.5	1.6	0.9	2.4	2.4	1.7	0.8	2.4	1.6	0.8	2.4
2004–2005	Mean	29.7	14.1	10.5	5.2	15.6	13.7	11.2	4.8	16.0	10.8	4.9	15.6
	SD	4.4	2.5	1.4	0.7	2.1	2.5	1.5	0.7	2.1	1.4	0.7	2.1
2005–2006	Mean	27.6	14.1	9.1	4.4	13.4	13.8	9.7	4.2	13.8	9.3	4.2	13.4
	SD	6.3	3.9	1.7	0.9	2.6	3.9	1.8	0.8	2.7	1.8	0.8	2.6
2006–2007	Mean	25.1	11.8	9.0	4.2	13.2	11.5	9.5	4.0	13.5	9.2	4.0	13.2
	SD	7.5	5.9	1.6	0.9	2.3	5.9	1.7	0.8	2.4	1.6	0.8	2.3
2007–2008	Mean	27.4	15.0	8.0	4.4	12.1	14.6	8.9	4.1	12.8	8.3	4.1	12.2
	SD	6.0	2.9	2.0	1.9	3.9	2.9	2.1	1.6	3.7	2.1	1.6	3.8
2008–2009	Mean	26.0	13.1	8.9	4.1	12.7	12.7	9.5	4.1	13.3	8.9	4.1	12.7
	SD	5.4	2.4	1.9	1.6	3.4	2.3	2.2	1.3	3.4	2.1	1.3	3.3
2009–2010	Mean	31.5	15.3	10.7	5.6	16.2	14.6	11.7	5.2	16.9	11.0	5.2	16.2
	SD	4.9	2.6	1.5	1.3	2.7	2.6	1.6	1.0	2.6	1.6	1.0	2.6
2010–2011	Mean	35.6	16.9	12.5	6.3	18.7	16.4	13.5	5.7	19.2	12.8	5.8	18.6
	SD	5.9	3.0	2.0	1.4	3.3	3.0	2.2	1.1	3.3	2.2	1.1	3.2
2011–2012	Mean	33.0	15.0	12.0	6.1	17.9	14.5	12.9	5.6	18.5	12.3	5.6	17.9
	SD	6.1	2.8	2.2	1.4	3.6	2.9	2.4	1.1	3.5	2.4	1.1	3.5
2012–2013	Mean	25.5	12.7	8.7	4.1	12.7	12.3	9.5	3.9	13.3	8.9	3.9	12.8
	SD	6.1	3.8	1.9	1.4	3.1	3.7	2.0	1.2	3.1	2.0	1.2	3.0
2013–2014	Mean	24.5	11.8	8.6	4.1	12.6	11.4	9.2	3.8	13.0	8.8	3.9	13.6
	SD	5.1	3.2	1.6	1.5	2.9	3.1	1.7	1.2	2.8	1.7	1.2	2.9
1997–2014	**Mean**	**30.2**	**14.9**	**10.4**	**4.9**	**15.3**	**14.5**	**11.1**	**4.6**	**15.8**	**10.7**	**4.6**	**15.3**
	SD	**6.6**	**3.9**	**2.6**	**1.6**	**3.8**	**3.8**	**2.7**	**1.3**	**3.8**	**2.7**	**1.3**	**3.8**

[a]Averages and standard deviation are calculated from midyear to midyear (see Table A1 in Appendix). Density and temperature boundaries are based on the long-term averages described in section 2.3. The green-shaded rows are based on transports from the multiple regression technique applied to the central mooring K9 (see section 3.2.3 and Table A4 in Appendix)

example, the LSW transport uncertainty is estimated at 1.0–1.1 Sv depending on the water mass definition, and thus for the sparsely covered periods (highlighted in green) the uncertainty would be 1.5 Sv.

Comparing the magnitudes of the different layer estimates for certain water masses, the differences are of the order of 1 Sv or less, meaning that the different layer definitions are within the error bounds (see section A3.2).

4.2. Transport Time Series

With the above described procedures applied to the full 5-day resolution data set we now have transport time series for individual depth layers, or water mass levels, respectively, which we will interpret in the following section. Due to the intense intraseasonal TRW's the transport time series are rather noisy, and we will use either low-pass filtering or modal decomposition by SSA to separate (low-frequency) signal from noise.

4.3. Modal Decomposition by SSA

Using this SSA technique, we obtained transport time series for LNADW and LSW (Figures 10a and 10b). These time series are dominated by short-term (days to weeks) fluctuations associated with topographic waves and other mesoscale features [*Fischer et al*., 2015] that may mask longer-term fluctuations and possible correlations among the records. These records are long enough to permit spectral analysis methods for evaluating the rather short time scales including seasonality, but they are not long enough to perform a spectral analysis for investigating multiannual to decadal variations. Further, the determination of linear transport trends crucially depends on the length and phase of the dominant fluctuations relative to the observational period, and may thus be leading to artificial trends.

For both layers—LNADW and LSW—the first eight modes have been used to decompose and reconstruct the time series from the modes. The sum of these modes explains 47 and 40% of the variance of the original (5-day resolution) transport time series. The rms-difference of the original transports minus the reconstructed is around 2.3 Sv for the LNADW layer and 2.5 Sv for LSW transports, and the residuals show Gaussian distributions with negligible skewness. This reflects that the SSA decomposition has successfully separated long-term variability from noise. Thus, it appears more appropriate to relate the variance of individual modes to the time series with already most of the intraseasonal noise removed, i.e., relative to a 90 day low-pass-filtered version of the time series.

The LNADW transport below 1850 m depth is dominated by the first and second modes which together explain 63% of the 90 day low-passed data. The mode 1 + 2 reconstruction has an oscillatory appearance with a period around 7–10 years, covering a transport range of around 5 Sv (2.5 Sv amplitude). The variance explained by the near-annual cycle (modes 4 and 5) accounts for 14% of the variance (relative to the 90 day low-passed record). Modes 7 and 8 contain intraseasonal variability at periods around 3 months (90 day). As a result, the modal decomposition by SSA acts as a very effective low-pass filter and the low-frequency transport fluctuations of LNADW can be sufficiently described by the first six SSA modes. Overall, the unresolved part of the transport is Gaussian and has a standard deviation of 0.8 Sv. There is a rather weak decline apparent in the reconstruction by the first two modes (1.1 Sv per decade), whereas the estimate for the full 5 day record yields a decline of 1.2 Sv per decade.

The LSW (in the depth range from 400 to 1850 m) shows a different behavior. This time series has long-term contributions concentrated in modes 1 and 4, explaining 41% of the variance of the 90 day low-passed record of LSW transport. These modes occur as individual components at separate frequencies. This means that the long-term variability in LSW transports is not represented by nonharmonic oscillations but instead is characterized by piecewise linear trends with decreasing transports in the first 5 years of the observations and a negligible trend from 2003 to 2012. Similar to the findings above, only the lowest six SSA modes are needed to explain 80% of variance found in the 90 day low-passed record, and modes 7 and 8 contain intraseasonal variance that might be treated as noise for investigating annual and longer time scales. Calculating a possible trend from either the reconstruction or the full record yields a linear decay of 2.6 Sv per decade, which comes from the fact that the time series ends with the weak part of a multiannual variation at the end of the time series. Truncating the LSW time series at its maximum in late 2010, such a trend would be around 1–2 Sv per decade only.

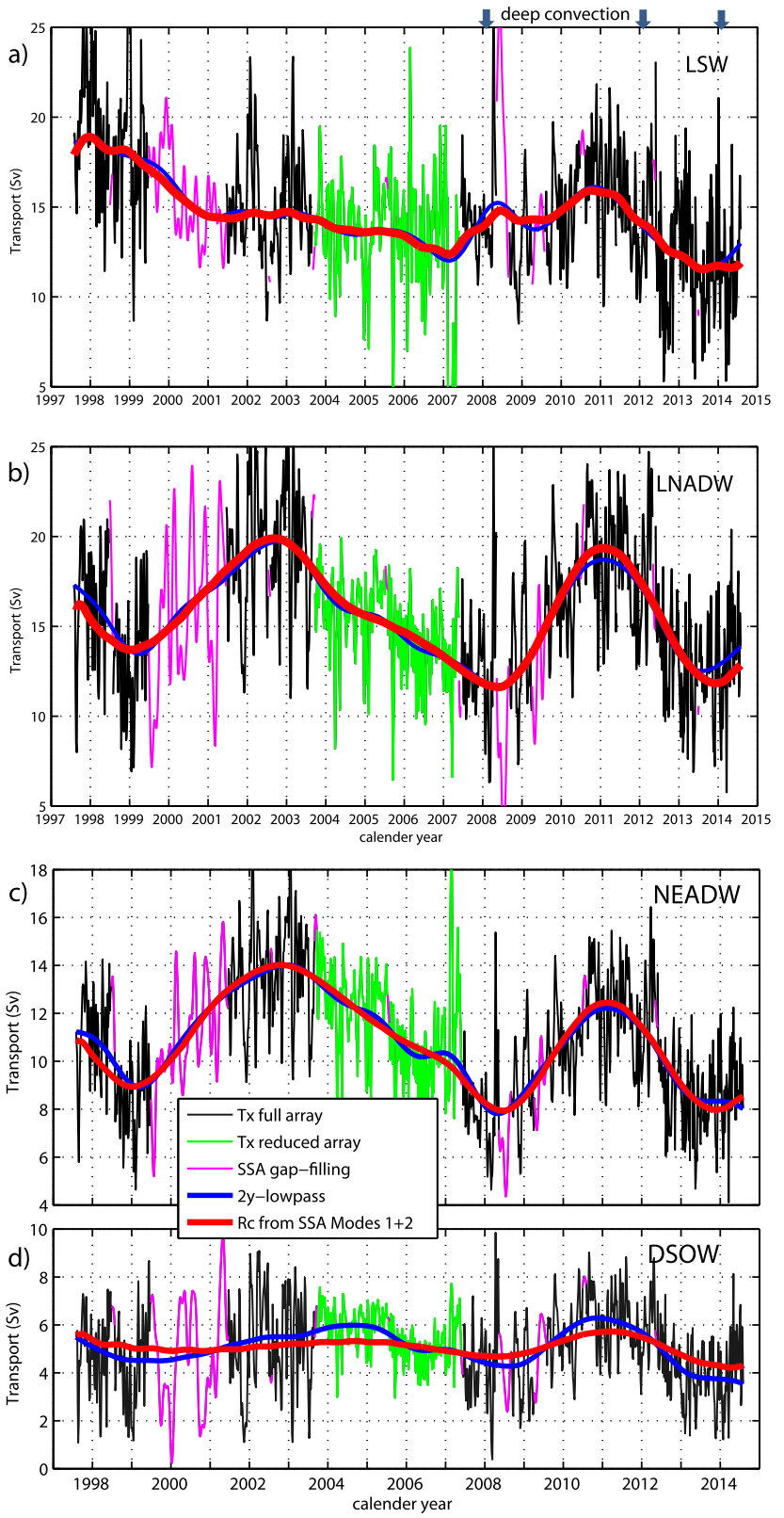

Figure 10. Export from the Labrador Sea at 5-day resolution and without gaps; black lines are for periods of full array coverage; green lines for periods with reduced coverage but with central mooring K9 in place, and magenta lines for gaps filled by SSA (EOF) modes. The low-frequency variation is dominated by a pair of SSA modes at quasi-decadal time scales. Overflow components are (c) NEADW extending from 1850 to 2800 m and (d) DSOW from 2800 m to the bottom.

Separating the LNADW variability by source region, i.e., the NEADW originating from the eastern sills, and the DSOW originating from Denmark Strait, it is apparent (Figure 10b) that the LNADW transport is dominated by the contribution from the eastern SPNA. Only one third of the LNADW transport is contained in the DSOW class. However, even in the DSOW layer there is some evidence of longer time scales in phase with the overlying NEADW. Because of the close proximity to the bottom, the uncertainty of the DSOW transport is larger and additionally the signal-to-noise ratio for the long-term fluctuations is larger than in the overlying layers.

Although the time series are too short for significance considerations in Fourier spectra, we used such spectra to determine the dominant frequencies and possible correspondence between layer transports. The DWBC reveals variability on various time scales, ranging from days to decades (Figure 11) and occurring in distinct frequency bands. The shortest periods are on intraseasonal time scales associated with locally forced topographic Rossby waves [*Fischer et al*., 2015]. Their period depends on the slope of the Labrador shelf break in the vicinity of the observational site. The TRWs span the entire depth range covering LSW and LNADW levels with somewhat higher energy levels in the LSW range.

While the shallow Labrador Current shows pronounced seasonality [*Kopte*, 2013], the deep flow has no distinct annual cycle but instead periods around 9 months (Figure 11) which are most evident in the LSW range. In fact, this is the strongest peak in the power spectrum, of unknown origin to us. An additional peak is present in both time series, near periods of 4 months. Covariance spectra show these two frequency bands as strong peaks, which likely indicate a more barotropic response of the DWBC in the intraseasonal time frame, in line with model findings by *Eden and Willebrand* [2001].

For longer periods the DWBC shows a large spectral gap on interannual time scales, which is most pronounced in the LNADW layer, where the SSA modes 1 + 2 are almost indistinguishable from the 1.5 year low-pass-filtered transport time series (Figure 10), illustrating that there is almost no variability in the time range from 1.5 to 8–10 year. This indicates that the deep SPNA acts as a band-pass to this frequency range, and this frequency band is also weakly present in the covariance spectrum. Another interannual band with some covariance is near the 24–30 month period, in this case more due to the LSW signal.

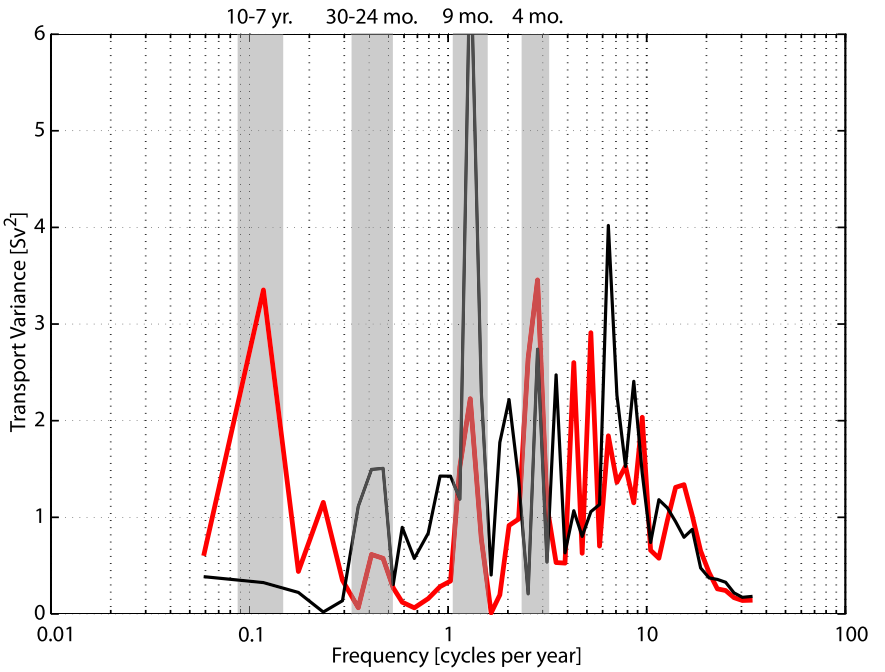

Figure 11. Power spectrum of transport variability for LSW export (black) and for LNADW export (red). No significance levels are given, as time series are short with respect to interannual variability. Gray shaded period range for covariance peaks—strongest cross correlation for intraseasonal peaks.

5. Transport Variability and Its Regional Connectivity

A 17 year long time series of volume transports is now available at the exit of the Labrador Sea. The 53°N observatory is located downstream of the central Labrador Sea convection area and it is here where the three components (LSW, NEADW, and DSOW) of the North Atlantic Deep Water merge into the DWBC. This enables us to briefly address a number of questions, such as

1. What is the source of the quasi-decadal variability dominating the LNADW export?
2. Is convection activity related to LSW transport variations within the DWBC?
3. Are barotropic and baroclinic contributions occurring in different frequency bands?

5.1. Quasi-decadal Variations and Their Origin

The origin of the large amplitude fluctuations of the overflow components (here summarized as LNADW) is one of the challenges that require future work. On long time scales the LNADW at the Labrador Sea exit is dominated by almost decadal transport fluctuations present in both overflow constituents, the NEADW and DSOW. The joint amplitude of these fluctuations is significant in comparison to their mean transport and they are large compared to the magnitude of the overflow source variability. What we know from simultaneous long-term investigations on the sills bounding the SPNA to the north is that both the northward warm water flow [*Berx et al*., 2013] and the two overflow components [*Jochumsen et al*., 2015] show no long-term trends. The components show interannual transport variability of the order of 1 Sv [*Berx et al*., 2013] but fluctuations near decadal periods are not evident.

As the sources, i.e., the overflows, exhibit no equivalent variability the quasi-decadal mode has to be imprinted downstream from the source regions within the SPNA—this is true for both amplitude and frequency. Furthermore, as both overflow components contribute to this signal, it has to be generated in the western part of the basin, where the colocation of the two allows for in-phase variability.

In order to relate the long-term transport variability to whatever forcing may generate the observed quasi-decadal variability, a brief discussion will follow. The large-scale atmospheric field of the area in question is represented by the North Atlantic Oscillation (NAO); here we use the winter NAO (DJFM) derived from the Sea Level Pressure difference between Lisbon (Portugal) and Reykjavik (Iceland) [*Hurrell and Deser*, 2009]. This index exists from 1864 to present, and thus covers not only the observational period but extends backward by many decades (Figure 12c shows the record from 1900 to 2015). The NAO contains several long time scales with the multidecadal and quasi-decadal periods as their dominant components. These can be separated by applying the SSA technique to the NAO time series with Mode 1 representing the multidecadal variability (may be also interpreted as a series of multiyear trends); while modes 2 + 3 represent a quasi-decadal mode that exists through most of the NAO record (Figures 12a and 12c).

This variability is reflected in many records, e.g., in sea level records of the subpolar Northeast Atlantic [*Jevrejeva et al*., 2006] and in various subpolar temperature records. Here we investigate whether the deep export out of the Labrador Sea shows a relation to the NAO. For this purpose we used the demeaned transport time series of Figure 10b divided by −2 to be comparable to the NAO index curve. A strong correspondence of the two time series and in-phase variability is evident, even though low NDF prohibit a determination of possible lags. Thus, the periods around 1999, 2008, and 2014 with less than average outflow from the Labrador Sea correspond to positive NAO phases, while periods around 2003 and 2011 show larger than average LNADW export which is associated with negative NAO signals.

This variability on decadal time scales also offers a possible explanation for the transport discrepancies at Cape Farewell, the southern tip of Greenland, mentioned in the introduction. While the LNADW transport was estimated by *Bacon and Saunders* [2010] at 9.0 Sv for 12 months in 2005–2006 and 13.3 Sv based on measurements in 1978, *Fischer et al*. [2010] found 15 Sv for the same density range for the time period 1997–2009, and our estimate for the updated time series 1997–2014 is 15.6 Sv. Such a range of transports is well within the measured decadal fluctuations which dominate the deep outflow from the Labrador Sea (see Figure 10b).

5.2. Boundary Current Export and Convection

Just recently, and after a decade of rather weak convection, the Labrador Sea experienced two extreme winters during which convection reached depths of more than 1500 m [*Yashayaev and Loder*, 2009; *Kieke and*

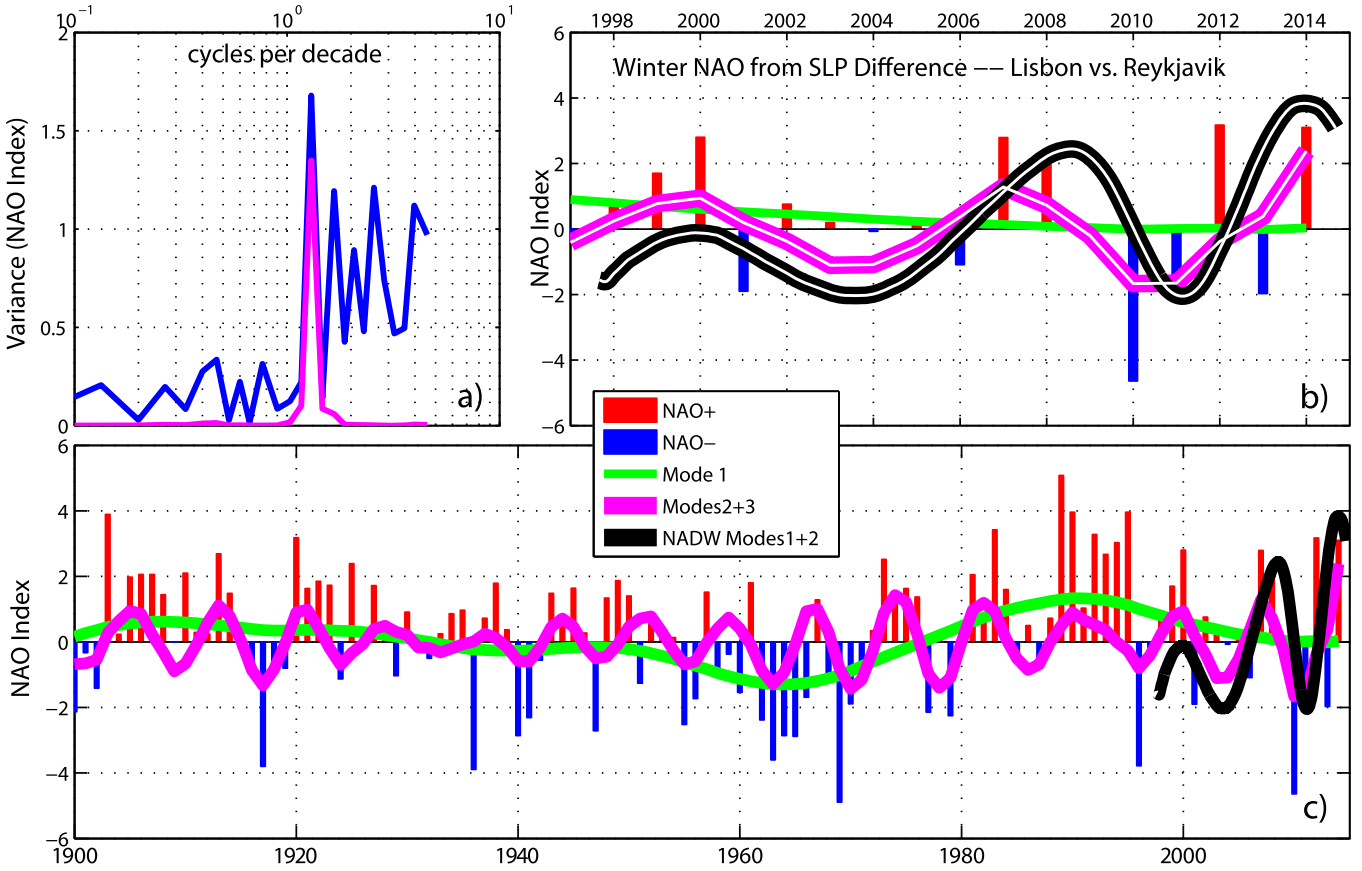

Figure 12. North Atlantic Oscillation index calculated from sea level pressure difference between Lisbon and Reykjavik for the time period 1900–2014. (a) Variance spectra of NAO index (blue) and SSA reconstruction modes 2 + 3 (magenta), both showing the quasi-decadal component. (b) Time series 1998–2014 of NAO index shown as annual values (red/blue), multidecadal SSA mode 1 (green), quasi-decadal SSA modes 2 + 3 (magenta). Also shown are the LNADW modes 1 + 2 from Figure 10b, demeaned and scaled by a factor of (−2), for comparison. (c) Same as Figure 12b but for 1900–2014.

Yashayaev, 2015] with increased formation of Labrador Sea Water. Observations in the central Labrador Sea by our moored station K1 clearly show that the upper and intermediate (LSW) layers warmed continuously during the last 20 years and even at 1500 m depth the water now is almost 1°C warmer than 20 years ago. This warming is at least partially interrupted by the events in 2008 and 2014; however, the temperature evolution in the boundary current differs from that in the basin center after 2008. The two winters are those with strong positive NAO phases that are responsible for the peaks in the SSA modes 2 and 3 (Figure 12). However, the transport time series of LSW export does not clearly reflect these cooling events marked at the top of Figure 10a.

5.3. Barotropic and Baroclinic Elements of the DWBC

Most striking is the difference of the transports across the deep water constituents (Figure 13) on long (quasi-decadal) time scales. Such a baroclinic behavior of the circulation has been discussed in the model study of *Eden and Willebrand* [2001] who diagnosed a delayed baroclinic NAO response of the subpolar circulation on time scales near 6.8 year periods.

A visual inspection of the transport time series reveals periods of intense and weak export of LNADW in the depth range below 1850 m or the corresponding density (see above). How these differences are reflected in the boundary current structure is another interesting question and it is clearly exhibited in the difference field. It is the deep velocity core that shows an overall increase or decrease between the phases. The largest difference is found at the offshore edge of the current core, suggesting that the core has stronger flow during the maximum phases and expands upward and offshore. The LSW layer reveals no significant changes in structure nor does it show flow anomalies coordinated with those of the LNADW layer.

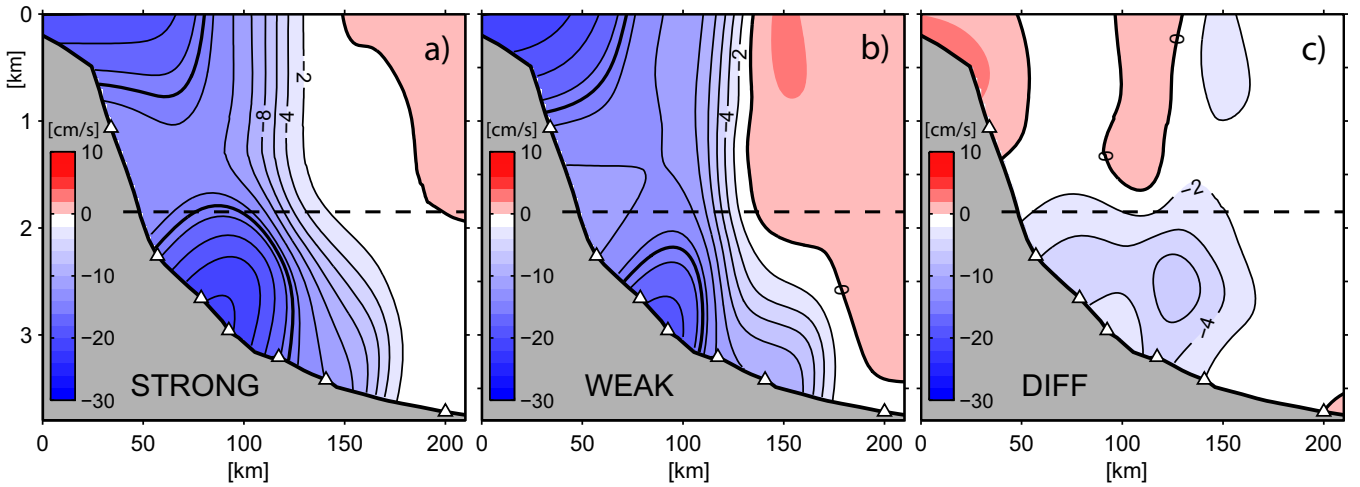

Figure 13. Difference of boundary current structure for phases with strong LNADW export (years: 2002, 2003, 2011, 2012) versus phases of weak LNADW export (years: 1998, 1999, 2008, 2009, 2013, 2014). Figure 13c is the difference of the extremes with large (up to 6 cm/s) values in the LNADW range, and small differences at the LSW levels. Mooring locations are indicated by triangles at the bottom; the dashed line is 1850 m depth.

This behavior of the boundary current contradicts the idea of a strong barotropic forcing contribution in the Labrador Sea. More likely the two layers (LNADW and LSW) got their long time scale variations imprinted at different locations and by different processes. It is beyond the scope of this paper to further investigate that in more detail; this should be done carefully in conjunction with additional data sources and realistic high-resolution modeling.

6. Discussion

The Deep Western Boundary Current at the exit of the Labrador Sea transports about 30 Sv of NADW out of the Labrador Sea, which is about twice the transport needed to supply the deep limb of the AMOC. This suggests that strong recirculation elements should exist within the subpolar regime—part of which is local within the narrow recirculation cells [*Lavender et al*., 2000; *Fischer and Schott*, 2002] adjacent to the boundary current while the larger fraction should supply the deep cyclonic circulation in the western subpolar gyre. We present methods to derive transport times series from a combination of direct current observations with variable coverage of the DWBC system (fully resolving array to single station coverage and even full gaps) in combination with less frequent LADCP station data.

We have shown that the quasi-decadal fluctuations in the North Atlantic Oscillation (NAO) appear related to those of the LNADW transport in the Labrador Sea Boundary Current (Figure 12). The NAO is the dominant atmospheric mode over the North Atlantic, and variations in the NAO are associated with strong changes in wintertime wind stress variations or "storminess" over the North Atlantic, and thus should have a major influence on the subpolar circulation. The NAO contains pronounced frequency bands and these are represented by just a few leading SSA modes that dominate the low frequency NAO variability (Figure 11). Within the context of this paper we are most interested in the well-known quasi-decadal NAO mode [*Deser and Blackmon*, 1993] that is also depicted in oceanic variations such as SLP variability in the North East Atlantic [*Jevrejeva et al*., 2006]. It should be mentioned, however, that the role of the NAO-related processes might be different for the time scales described herein. *Woollings et al*. [2015] analyzed the NAO and related effects on climate relevant parameters by demonstrating clear physical differences between NAO variability on interannual-decadal (<30 year) and multidecadal (>30 year) time scales. It is shown that on the shorter time scale the NAO is dominated by variations in the latitude of the North Atlantic jet and storm track, whereas on the longer time scale it represents changes in their strength instead.

Several feedback mechanisms between oceanic variability and quasi-decadal NAO variations have been discussed on the basis of observations and climate modeling [*Reintges et al*., 2016]: (a) between SST and wind-driven circulation; (b) between NAO and AMOC, and (c) through projections of SST anomalies back on the NAO.

Herein, we show for the first time a deep circulation element that is in phase with the quasi-decadal NAO mode; and as we believe that the LNADW transport within the DWBC is key to the AMOC, this behavior of the deep subpolar circulation might be representative of linking NAO, DWBC, and AMOC on quasi-decadal time scales.

In conclusion it appears that the Boundary Current off Labrador is not the uniform circulation element that has been assumed to exist. Although the circulation is cyclonic across all depth levels, the Boundary Current consists of four elements that—at least on interannual and longer time scales—behave independently. These elements are the Labrador Current extending down to 500 m water depth at the shelf edge, the LSW range of the DWBC sometimes called the Deep Labrador Current (DLC) [*Lazier and Wright*, 1993], a deep current core comprising the overflow part of the DWBC and containing strong decadal variations generated elsewhere (presumably in the open SPNA), and finally a recirculation cell as the offshore limit of the DWBC. Recirculation is found to terminate the DWBC at various places in the Labrador Sea, namely at 53°N and north of Hamilton Bank at the western side of the basin [*Hall et al*., 2013] and on the eastern side of the basin terminating the West Greenland Current. The recirculation intensity appears to be quite different when comparing the estimates north of Hamilton Bank with those at 53°N, and this might be an indication that there are individual recirculation cells as suggested by *Lavender et al*. [2000].

Local forcing apparently influences the shorter periods of less than a year with a barotropic contribution, and this corresponds to the findings of *Eden and Willebrand* [2001] that the bulk of the variability of the oceanic circulation is related to the North Atlantic Oscillation (NAO). Realistic experiments and idealized sensitivity studies with their model show a fast (intraseasonal time scale) barotropic response and a delayed (time scale about 6–8 years) baroclinic oceanic response to the NAO. Although we are not able to detect any delay with respect to the corresponding NAO variability that was suggested by *Eden and Willebrand* [2001], our findings indicate that on interannual to decadal time scales the deep boundary current system in the Labrador Sea is rather baroclinic. However, the quasi-decadal transport variability is more likely generated outside the Labrador Sea in the open subpolar North Atlantic through NAO-related forcing. Subsequent fast signal propagation along the western shelf break of the subpolar North Atlantic might explain the lack of a significant phase lag between NAO and LNADW transport at the exit of the Labrador Sea. At present we can only speculate about the reasons for the inverse response of the deep flow to the NAO variability. The close temporal correspondence of the processes suggests that the deep response is due to fast dynamic processes (waves) rather than thermohaline processes but a more detailed investigation to address this question in conjunction with other elements of the subpolar circulation will be the subject of forthcoming investigations.

At present and in the near future, these objects will be addressed in more detail, as the 53°N observatory will be continued as a contribution to the international *OSNAP* [*Lozier et al*., 2016] program. One of the associated key questions is to investigate how the subpolar AMOC might react on varying intensities of convection and deep water production. Observational evidence for such a linkage has been weak, i.e., no clear indication of such a response. However, with the deepening Labrador Sea convection in recent years (I. Yashayaev, personal communication, 2016), the timing of these measurements is exciting and provides strong motivation to sustain the observing activities.

Appendix A

A1. Sensitivity of Transport Calculations

The uncertainty of the LADCP transport was tested by applying a Monte Carlo variation technique by repeatedly selecting a random sample of about two thirds of the available 150 LADCP profiles (approximately 100 profiles from the full time period, see Table A1 for the inventory of CTD sections). This was done by generating a random sequence of prescribed length and varying between 0 and 1. This was then multiplied by 150 and transformed to an array index (integer numbers between 1 and 150). This guarantees that data were picked from the entire time period and not just from the beginning or end of the data set. Then the reduced data set was gridded, using the same weights as for the full field. This gridded field was then integrated for transports in the DSOW depth range (2800 m to the bottom), the NEADW depth range (1850–2850 m) and finally for the total NADW range below 500 m depth. This procedure was repeated 200 times, and besides the transport estimates we also saved the number of profiles used, plus an indicator whether the data used were more from the later cruises or the earlier ones. A second 200-member run was performed by using even less data (∼50%).

Table A1. Inventory of CTD and LADCP Data Available at the 53°N Section[a]

Section	Year/Month	Ship/Cruise	Stations
1	1996/Jul	Valdivia 161	70-77
2	1997/Jul	Meteor 39/4	14-21
3	1998/Jul	Valdivia 172	
3	1999/Jul	Meteor 45/3	02-14
4	2001/May	Meteor 50/1	
5	2001/Jun	Meteor 50/2	11-14
6	2003/Sep	Meteor 59/3	23-30
7	2005/Jul	Thalassa wna05	16-29
8	2007/Jun	Merian 05/2	03-21
9	2008/Aug	Merian 09/2	01-17
10	2009/May	Merian 12/1	03-14
11	2010/July	Meteor 82/1	
12	2012/May	Merian 21/1a	Two occupations
13	2014/Aug	Thalassa MSM40	

[a]These 13 sections were used to construct the hydrographic background and the LADCP-based currents to supplement the moored data.

The result is a probability distribution of the transport estimates together with mean and standard deviation and the most frequent transport value. In all cases the mean value is close to the most frequent value, the skewness is small, and the property distribution (transport of water masses) is near Gaussian. The range of transports in each of the classes increased when less input data are used—see the standard deviation in Table A2. This can be compared to the transport value calculated from all 150 profiles—first line of Table A2.

Summarizing, we demonstrate that the LADCP measurements allowed an estimate of the transports of the deep water components as listed in the SD rows of Table A2 at 60% significance (multiplying this by a factor of 2 gives the 95% significance). We conclude that the mean deep water export out of the Labrador Sea at 53°N can be estimated with an accuracy of about 10% of the mean from this number of profiles/sections.

A2. Determination of Transport Uncertainties From Moored Array Data

In this paper we generated a set of transport time series from current meter and shipboard data with different instrumental coverage and thus with different uncertainties. These uncertainties arose from a variety of input sources, their temporal and spatial distribution and techniques involved in the processing. Users of these data should be aware of the error sources and their magnitude. For example the overflow measurements in Denmark Strait constructed by only one or a few ADCP's [*Jochumsen et al.*, 2015] have different sources of uncertainties than the multi-instrument arrays of the RAPID or 53°N mooring efforts. Further, it would be important to relate the uncertainties to the processes that are investigated. Here we are interested in the low-frequency evolution of the DWBC as part of the AMOC variations, and as such we will discuss the uncertainties for the time scales of interest, rather than applying some general broadband noise consideration (e.g., standard error of mean). Typical error sources are

1. Measurement errors—do they matter?
2. Intraseasonal variability and its impact on interannual and longer transport determination
3. Mapping uncertainties—the role of spatial scales, vertical and horizontal
4. How well-defined are water mass boundaries?
5. Combining uncertainty estimates

A2.1. Measurement Errors: Do They Matter?

Generally each current meter has its inherent deficiencies, and there may be system immanent uncertainties which are quite severe in some cases. Let us consider an array of RCM current meters and a predominant flow direction. As long as we have sufficient flow everything is smooth—we have calibration coefficients to transfer rotor evolutions to current speed in a linear way. Once the flow ceases rotors become stalled and friction hinders a smooth restart of rotor revolution—this leads to a bias that is not predictable, as it depends on the flow itself. For the RCM records used herein, the background flow was stable and rather large, such that regular stalled periods associated with tidal flow variability did not occur. The same zero-bias in mechanically current meters can be caused by biofouling in biologically productive regions—less likely and not reported in the measurements herein. In individual

Table A2. LADCP-Based Transports of Water Masses and Their Uncertainties Derived From Monte Carlo Simulations

	NADW (Sv)	NEADW (Sv)	DSOW (Sv)	LSW (Sv)
Total (100%)	31.0	10.7	4.3	16.0
mf-val (65%)[a]	31.2	11.0	4.0	16.1
mf-val (50%)[a]	30.2	11.0	4.0	15.9
Mean (65%)	31.1	10.8	4.3	16.0
Mean (50%)	31.0	10.8	4.4	15.9
SD (65%)	1.8	0.4	0.4	1.0
SD (50%)	2.6	0.7	0.7	1.5

[a]Most (frequent) probable value.

cases with rather long (months) periods of stalled rotors, the data have been eliminated before transports were derived.

Another effect reported from some brands of the single point Doppler current meters where a depletion of scatterers in the deep ocean leads to enhanced noise levels in the velocity data. In this case, biases, generally toward small Doppler shifts, cannot be excluded; thus, velocity records will be biased toward low speed.

Additionally the acoustic current meters used herein are mounted in line and may be subject to strong inclination angles (in excess of 20°) affecting both the mean flow and introducing high-frequency noise. This was mainly overcome by designing rather stiff moorings with only small vertical excursions and thus small instrument inclinations.

Then there are errors for individual instruments which in the best case can average out when using many instruments with random inconsistencies. One of the constraints in designing such an array would be to avoid rotor current meters in low current environments and Doppler current meters in low scatter regimes—thus a careful instrument distribution would minimize the risk of measurement biases. Therefore, we assume measurement errors to be negligible compared to the other error sources.

A2.2. The Impact of High-Frequency Noise on Transport Determination: ϵ_1

Signal/SNR/$\sqrt{(N-1)}$. This signal-to-noise ratio (SNR) is similar for each of the water masses and the total NADW. With an integral time scale of 6 months, the resulting NDF (number of degrees of freedom) is the length of the time series divided by the integral time scale, i.e., NDF = 17 year/0.5 year = 34, thus the factor is 5.7 and the resulting uncertainty of this LNADW transport fluctuation is 0.6 Sv.

The high-frequency part of the DWBC velocity field is dominated by topographic Rossby waves that are trapped at the steep slopes of the shelf break [*Fischer et al*., 2015]. Their frequency depends on topographic Beta and the latitude at which they occur. Thus, the frequency band contaminated by this variability varies along the path of the DWBC. Here at 53°N with its rather steep shelf break, the dominating periods are in the range of days to weeks.

To illustrate the influence of the intraseasonal variance (noise in this case), we summarize the standard deviation for periods less than 3 months (or 90 days) for all three water masses (where the NADW is the sum of LSW and LNADW) in the following Table A3.

Thus, the frequency band associated with the TRWs (noise) and long-term variance (signal) comprise about the same variability and the signal-to-noise ratio would be 1. If we would like to determine the magnitude of say the LNADW multiannual transport fluctuations, the uncertainty of this estimate (Table A3) would be

$$\epsilon_1 = 2 \times \text{noise} / \sqrt{(\boldsymbol{N}-1)}.$$

This noise is similar for each of the water masses and the total NADW. With NDF (number of degrees of freedom) estimated from the duration of the time series, and divided by the time scale separating noise from signal yields (i.e., NDF = 17 year/0.25 year = 68), the factor would be around 8 and the resulting uncertainty (95% significance) of the multiannual LNADW transport fluctuations would be 0.7 Sv. Similar values are obtained for the LSW.

A2.3. Mapping the Currents: The Role of Horizontal Scales, ϵ_2

During times with a full coverage of the array, transports were calculated by interpolating the measured current on a regular small scale grid. We choose a Gaussian interpolation scheme that proved to be satisfactory during previous analyses [*Dengler et al*., 2006]. Then the currents were integrated horizontally and vertically in predefined layers. These layers could either be depth layers, density ranges or bounded by isotherms. This procedure has been described earlier, and we briefly investigate how accurately the original measured data are represented in the gridded fields by instead reinterpolating the gridded field back to the original positions. Varying the interpolation scales led to smoother (larger scales) or more variable (smaller scales) current fields, while the total layer transports are only lightly affected.

The difference between input data and interpolated field can then be statistically evaluated. For each of the layers we calculate a RMS deviation of the interpolated relative to the original field. The RMS value can then be compared to the average flow of the layer and subsequently to the transport in the respective layer. In the interior of the DWBC the resulting uncertainty of an annual mean transport is about 5%, which translates to 0.8 Sv for either the LNADW or the LSW. A little larger deviation (original versus interpolated) is

Table A3. Standard Deviation of Transport Time Series in Different Frequency Ranges

SD (Sv)	Full Record	Low Freq. (>90 Days)	High Freq. (<90 Days)
LSW	4.2	2.5	3.0
LNADW	4.2	2.9	2.8
NADW	6.4	4.0	4.6

found for instrument locations close to the bottom, where the currents are strong and the spatial scales are small. This would lead to somewhat increased inaccuracies in the DSOW layer transports (10% of the mean DSOW transport; i.e., 0.5 Sv).

A2.4. How Well-Defined Are Water Mass Boundaries? ϵ_3

Suppose the water mass boundaries are defined by isopycnals measured during the service cruises, i.e., every other year, and their mean location is as shown below. A second assumption is that the deep isopycnals are not reached by fluxes from the surface (i.e., no deep convection). Then the LNADW layer between $\sigma_\theta = 27.80$ and the bottom is about 1500 m thick, and the density change from the first half of the time series to the second half of the time series is mainly less than 0.01 σ_θ units. In the transition area between LNADW and LSW a σ_θ change of 0.01 corresponds to a ~100 m shift of the boundary, an uncertainty well within the variability shown in Figures 5b and 5c.

However, in each of the realizations we have an impact of geostrophic modifications at various time scales that will lead to significant aliasing effects. The first contribution is due to the influence that TRW's have on the density field. Their time scales of the order of a few weeks suggest that any hydrographic survey (duration of a few days) is a nonsynoptic snapshot of the density (hydrography) field. Their effect cannot be separated from the longer-term variability as is possible for the current measurements of the mooring records.

On even longer time scales—here we consider time scales longer than a year; individual sections are synoptic with respect to these time scales. Undersampling these time scales will again lead to aliasing, as all of these fluctuations are predominantly geostrophic and modify the density field accordingly.

What can be done about this? At each station location we calculated the statistics of the isopycnal depths and determined its scatter. In the best case, the mean location of the water mass boundary between LSW and LNADW can be determined at an accuracy of about 50 m (see Figure 5b)—this is estimated from the standard deviation (150 m) divided by the square root of degrees of freedom

$$\sqrt{NDF} = \sqrt{(N-1)} \sim 3; \quad \text{with N the number of ship sections contributing to the estimate.}$$

Given an invariant current field the resulting thickness uncertainty 50 m versus 1500 m as the total thickness of each water mass would transfer into a transport uncertainty of the order of 3%. For the typical LNADW transport of 16 Sv the resulting uncertainty due to layer thickness would be 0.5 Sv for each of the water masses. Note transports within depth layers are not affected, and thus the uncertainties for depth layer transports are somewhat smaller. The same is true for the full NADW transport from 400 m down to the bottom.

Here we assumed that the density field shows no systematic variations in time which is in conflict with the observed temporal evolution of σ_θ compared to σ_2, with the latter showing no temporal dependence (Figure 5b). However, $\sigma_\theta = 27.80$ is the most often used isopycnal boundary for separating LSW from the underlying LNADW. This isopycnal shows a vertical migration toward shallower depth from the first half of the observing period to the second, and that would lead to an increase of LNADW transport and a corresponding LSW transport decrease of the order of 1 Sv per decade, while from the currents alone there would be no trend. Interestingly, when using the mean isopycnal location as the water mass boundary there is no significant difference between the three estimates. Thus, the preferred boundary separating LSW from LNADW is either defined by the mean location of $\sigma_2 = 36.95$ or by depth layers (here 1850 m).

Table A4. Gain Factors for Multiple Regressions Between Individual Current Meter Records and Full-Array Transports[a]

Water Mass	A1 (200 m)	A2 (1100 m)	A3 (1500 m)	A4 (2800 m)	rms	Correlation Coefficient
LSW	−0.1042	0.9961	−0.7831	1.2218	5.04	0.521
NEADW	0.0628	−0.1775	0.1023	0.4364	1.70	0.664
DSOW	−0.0383	−0.0383	0.0160	0.2380	1.53	0.297

[a]These gain factors are used to approximate full transports in water mass classes when only the central mooring K9 was in place.

Table A5. Basic Statistics for Gappy (Raw) and Filled Transport Time Series[a]

	LSW (Sv)		LNADW (Sv)	
Statistics For	Raw	Filled	Raw	Filled
Mean	14.5	14.8	15.6	15.5
Standard Dev.	3.8	3.7	3.8	4.0
Skewness	0.1	0.3	0.2	0.3
Kurtosis	4.9	5.0	2.9	2.9

[a]The numbers verify that the SSA gap-filling technique does not alter the basic statistics of the original time series (see section 3.2.4).

In T/S space there is a clear separation between Labrador Sea Water and the underlying Lower North Atlantic Deep Water. These two water masses contribute about the same volume transport in the DWBC. The signature of the water mass boundary is strongest after the end of the convection period in the early 1990s and weakens during the decade thereafter.

The deeper layers (NEADW, DSOW) have not been affected by winter convection during the past 20 years and there are no seasonal biases evident [*Kopte*, 2013]; however, the layers above are subject to seasonal variations due to winter mixing. This is especially the case for the upper bound of Labrador Sea Water and the inter-LSW level separating upper from classic LSW. An additional source of variability is due to the seasonal variations of the Labrador Current, leading to a geostrophic modification of the density field (and the isotherms). The timing is somewhat different from the convection induced changes, as the driving mechanism is the enhanced wind stress curl during winter (December/January). This extends far into the LSW, but not down to the boundary between LSW and LNADW.

A2.5. Combining Uncertainty Estimates

The total uncertainty for a layer transport is estimated from the individual error contributions using the rules for error propagation. This must be done for the individual fractions of the time series. In the case of the fully equipped array we estimate the uncertainty for the LNADW transport defined between $\sigma_2 = 36.95$ and the seafloor as

$$\varepsilon_{\mathrm{LNADW}} = \sqrt{\sum_{1}^{n} \varepsilon \boldsymbol{i}^2} = \sqrt{\left(0.6^2 + 0.8^2 + 0.5^2\right)} = 1.1 \ \boldsymbol{Sv}.$$

In the case of using depth layers as water mass boundaries the inaccuracy introduced by the density field must not be taken into account, which would reduce the uncertainty to 1.0 Sv. Similar error considerations can be made for each individual water mass, e.g., for LSW with similar uncertainties. For the total NADW range the uncertainty would be around 1.6 Sv.

For those periods with a reduced array (only the central mooring was available) we used another technique to project the currents from the central mooring to the full transport time series (Table A4). This resulted in larger scatter compared to periods with a full array—basically the noise of the transport time series increased considerably, and a crude estimate of the uncertainties for these periods yields uncertainties of ~1.5 Sv for annual means of the respective water mass; the assumption thereby is that the regression uncertainty is of the same order as the combined uncertainty for the fully instrumented array. An error estimate for the gappy part of the time series is not performed. Statistics for the gappy and filled transport time series are shown in Table A5.

For longer time scales, some of the uncertainties are slightly reduced (see Table A3) but the overall result is that uncertainties of the water mass transports are on the order of 5–10% of their mean, and this accuracy could only be achieved with a fully equipped array and the appropriate temporal resolution that is required to separate intraseasonal noise from climate relevant signals.

Finally, for the very long time scales we might experience an effect of mixing up long-term oscillations and trends. As these time series are long with respect to seasonal variations and shorter, they are short records with respect to decadal variability and long-term trends. With such a dominant multiannual variability as seen here, a trend determination crucially depends on the phase of the time series with respect to its dominant oscillations. In the case described here we may get trends even with sign changes, depending on when the observations began relative to the quasi-decadal mode of variability. However, with the SSA method we were able to separate oscillations, trend, and noise.

Acknowledgments

The research leading to these results has received funding from the German Ministry of Research and Education (RACE Program), and the European Union's Seventh Framework Program (FP7/2007-2013) under grant agreements 212643 (THOR) and 308299 (NACLIM). The data used in this analysis are available through the OceanSITES portal (www.oceansites.org). We appreciate the constructive comments by numerous colleagues and both anonymous reviewers.

References

Bacon, S., and P. M. Saunders (2010), The deep western boundary current at Cape Farewell: Results from a moored current meter array, *J. Phys. Oceanogr.*, *40*, 815–829.

Berx, B., B. Hansen, S. Østerhus, K. M. Larsen, T. Sherwin, and K. Jochumsen (2013), Combining in situ measurements and altimetry to estimate volume, heat and salt transport variability through the Faroe–Shetland Channel, *Ocean Sci.*, *9*, 639–654, doi:10.5194/os-9-639-2013.

Böning, C. W., M. Scheinert, J. Dengg, A. Biastoch, and A. Funk (2006), Decadal variability of subpolar gyre transport and its reverberation in the North Atlantic overturning, *Geophys. Res. Lett.*, *33*, L21S01, doi:10.1029/2006GL026906.

Dengler, M., J. Fischer, F. A. Schott, and R. Zantopp (2006), Deep Labrador Current and its variability in 1996-2005, *Geophys. Res. Lett.*, *33*, L21S06, doi:10.1029/2006GL026702.

Deser, C., and M. L. Blackmon (1993), Surface climate variations over the North Atlantic Ocean during winter: 1900-1989, *J. Clim.*, *6*, 1743–1753.

Eden, C., and J. Willebrand (2001), Mechanism of interannual to decadal variability of the North Atlantic circulation, *J. Clim.*, *14*(10), 2266–2280, doi:10.1175/1520-0442(2001)014<2266:MOITDV>2.0.CO;2.

Fischer, J., and F. A. Schott (2002), Labrador Sea Water tracked by profiling floats—From the boundary current into the open North Atlantic, *J. Phys. Oceanogr.*, *32*, 573–584.

Fischer, J., F. Schott, and M. Dengler (2004), Boundary circulation at the exit of the Labrador Sea, *J. Phys. Oceanogr.*, *34*, 1548–1570.

Fischer, J., M. Visbeck, R. Zantopp, and N. Nunes (2010), Interannual to decadal variability of outflow from the Labrador Sea, *Geophys. Res. Lett.*, *37*, L24610, doi:10.1029/2010GL045321.

Fischer, J., et al. (2015), Intra-seasonal variability of the DWBC in the western subpolar North Atlantic, *Prog. Oceanogr.*, *132*, 233–249, doi:10.1016/j.pocean.2014.04.002.

Ghil, M., et al. (2002), Advanced spectral methods for climatic time series, *Rev. Geophys.*, *40*(1), 1–41, doi:10.1029/2000RG000092.

Hall, M., D. Torres, and I. Yashayaev (2013), Absolute velocity along the AR7W section in the Labrador Sea, *Deep Sea Res., Part I*, *72*, 72–87, doi:10.1016/j.dsr.2012.11.005.

Hansen, B., and S. Østerhus (2007), Faroe Bank Channel overflow 1995–2005, *Prog. Oceanogr.*, *75*, 817–856, doi:10.1016/j.pocean.2007.09.004.

Hansen, B., H. Hátún, R. Kristiansen, S. M. Olsen, and S. Østerhus (2010), Stability and forcing of the Iceland-Faroe inflow of water, heat, and salt to the Arctic, *Ocean Sci.*, *6*, 1013–1026, doi:10.5194/os-6-1013-2010.

Hurrell, J. W., and C. Deser (2009), North Atlantic climate variability: The role of the North Atlantic Oscillation, *J. Mar. Syst.*, *78*(1), 28–41.

IPCC (2013), *Climate Change 2013: The Physical Science Basis. Contribution of Working Group I to the Fifth Assessment Report of the Intergovernmental Panel on Climate Change*, edited by T. F. Stocker et al., 1535 pp., Cambridge Univ. Press, Cambridge, U. K., doi:10.1017/CBO9781107415324.

Jevrejeva, S., A. Grinsted, J. C. Moore, and S. Holgate (2006), Nonlinear trends and multiyear cycles in sea level records, *J. Geophys. Res.*, *111*, C09012, doi:10.1029/2005JC003229.

Jochumsen, K., D. Quadfasel, H. Valdimarsson, and S. Jónsson (2012), Variability of the Denmark Strait overflow: Moored time series from 1996–2011, *J. Geophys. Res.*, *117*, C12003, doi:10.1029/2012JC008244.

Jochumsen, K., M. Köllner, D. Quadfasel, S. Dye, B. Rudels, and H. Valdimarsson (2015), On the origin and propagation of Denmark Strait overflow water anomalies in the Irminger Basin, *J. Geophys. Res. Oceans*, *120*, 1841–1855, doi:10.1002/2014JC010397.

Kieke, D., B. Klein, L. Stramma, M. Rhein, and K. P. Koltermann (2009), Variability and propagation of Labrador Sea Water in the southern subpolar North Atlantic, *Deep Sea Res., Part I*, *56*(10), 1656–1674.

Kieke, D., and I. Yashayaev (2015), Studies of Labrador Sea Water formation and variability in the subpolar North Atlantic in the light of international partnership and collaboration, *Prog. Oceanogr.*, *132*(3), 220–232, doi:10.1016/j.pocean.2014.12.010.

Kondrashov, D., and M. Ghil (2006), Spatio-temporal filling of missing points in geophysical data sets, *Nonlinear Processes Geophys.*, *13*, 151–159.

Kopte, R. (2013), Seasonal variations of the Deep Western Boundary Circulation in the subpolar North Atlantic Ocean—Observations in comparison with model data, MS thesis, 72 pp., Christian-Albrechts Univ. Kiel, Kiel, Germany.

Lavender, K. L., R. E. Davis, and W. B. Owens (2000), Mid-depth recirculation observed in the interior Labrador and Irminger seas by direct velocity measurements, *Nature*, *407*, 66–69, doi:10.1038/35024048.

Lazier, J. R. N., and D. G. Wright (1993), Annual velocity variations in the Labrador Current, *J. Phys. Oceanogr.*, *23*, 659–678.

Lozier, S., et al. (2016), Overturning in the subpolar North Atlantic Program: A new international ocean observing system, *Bull. Am. Meteorol. Soc.*, *97*, doi:10.1175/BAMS-D-16-0057.1, in press.

Marshall, J., and F. Schott (1999), Open-ocean convection: Observations, theory, and models, *Rev. Geophys.*, *37*, 1–64.

Reintges, A., M. Latif, and W. Park (2016), Sub-decadal North Atlantic Oscillation variability in observations and the Kiel climate model, *Clim. Dyn.*, *47*, 1–13, doi:10.1007/s00382-016-3279-0.

Rhein, M., D. Kieke, and R. Steinfeldt (2007), Ventilation of Upper Labrador Sea Water, 2003-2005, *Geophys. Res. Lett.*, *34*, L06603, doi:10.1029/2006GL028540.

Vautard, R., P. Yiou, and M. Ghil (1992), Singular-spectrum analysis: A toolkit for short, noisy chaotic signals, *Physica D*, *58*, 95–126.

Woollings, T., C. Franzke, D. L. R. Hodson, B. Dong, E. A. Barnes, C. C. Raible, and J. G. Pinto (2015), Contrasting interannual and multidecadal NAO variability, *Clim. Dyn.*, *45*, 539–556, doi:10.1007/s00382-014-2237-y.

Xu, X., H. E. Hurlburt, W. J. Schmitz Jr., R. Zantopp, J. Fischer, and J. J. Hogan (2013), On the currents and transports connected with the Atlantic meridional overturning circulation in the subpolar North Atlantic, *J. Geophys. Res.*, *118*, 502–516, doi:10.1002/jgrc.20065.

Yashayaev, I., and J. W. Loder (2009), Enhanced production of Labrador Sea Water in 2008, *Geophys. Res. Lett.*, *36*, L01606, doi:10.1029/2008GL036162.